Construction and application of a technical platform for determining cell cycle- and autophagy-associated cellular accumulation of lipid-based nanoparticles

Yisha Wang[1,2†], Gan Luo[1,2†], Haiyang Wang[1,2†], Yue Zheng[1,2], Xiao Xu[3], Wenbin Zhou[1,2], Junrong Lin[1,2], Baocheng Chen[1,2], Yifeng Jin[1,2], Meihua Sui[1,2*]

[1]*School of Basic Medical Sciences, Zhejiang University School of Medicine, Hangzhou, China*

[2]*Cancer Center, Zhejiang University, Hangzhou, China*

[3]*Department of Hepatobiliary and Pancreatic Surgery, People's Hospital of Hangzhou Medical College, Hangzhou, China*

†Equal contribution

[*]**Corresponding author**

Meihua Sui, M.D., Ph.D. **E-mail**: suim@zju.edu.cn

Abstract

Cellular accumulation of biomedical nanoparticles could be affected by cellular biological properties. However, little is known about the influence of cell cycle and autophagy on nanoparticle accumulation. What's even more tough is that several long-lasting methodological barriers have hampered the experimental performance and restricted related research progress. Herein, a multi-functional platform was constructed for simultaneously overcoming existing obstacles by integrating several technical approaches, particularly mitotic shake-off, for thorough cell cycle phase separation. Strikingly, application of this platform revealed that G2-phase and M-phase cells, two cell populations previously muddled up together as G2/M-phase cells, respectively exhibited the maximum and minimum accumulation of lipid-based nanoparticles. Moreover, although further verification is needed, we have provided a novel line of evidence for enhanced nanoparticle accumulation by autophagy blockade. Besides providing a technical solution, this study discovered characteristic cell cycle- and autophagy-associated nanoparticle accumulations that may offer new insights for optimization and application of nanomedicines.

Introduction

Leveraging the distinctive surface and size effect, nanodrugs have a wide range of applications in biomedicine[1]. Among a variety of nanocarriers, lipid-based nanoparticles, e.g. liposomes (LIP) and lipid nanoparticles (LNP), serve as exemplary carriers for successful clinical translation[2]. For instance, Doxil®, doxorubicin utilizing LIP as the carrier, is the first nano-sized drug approved for patients[3]. BNT162b2, the first LNP-delivered mRNA vaccine, is extensively used worldwide[4]. It has been noted that nanoparticle accumulation could be affected by key cellular biological properties. Cell cycle, a fundamental life process of mammalian cells, is critically involved in the onset, development, treatment response and prognosis of many diseases[5]. Particularly, proliferating tumor cells inside tumor tissues are distributed at distinct cell cycle phases, which is called cell cycle heterogeneity[6,7]. Given that studies from our team and others demonstrate that tumor cells possess cell cycle-dependent sensitivity to a variety of treatments including nano-drugs, cell cycle heterogeneity has been considered as a big challenge for antitumor therapy[6-12].

Nevertheless, so far only three literatures explored the impact of cell cycle on the retention of inorganic nanoparticles including CdTe QDs[13,14] and ZnO[15]. Regarding organic nanoparticles, five literatures respectively investigated the cell cycle-associated accumulation of carboxylated polystyrene nanoparticles (PS-COOH), FITC-dextran fibroin-encapsulated microspheres, cRGD-targeting matrix metalloproteinase-sensitive nanoparticles (FITC@NPs-cRGD), folate modified poly (L-amino acid) micelles and Tat/pGL3-Ca^{2+} nanoparticles[16-20]. It is noteworthy that several methodological limitations may interfere with the accuracy of data and result in the discrepant findings previously reported. For instance, the methods used or available in literatures could not differentiate between G2-phase and M-phase cells in physiological state[13-20]. Additionally, cell dissociation agent such as trypsin[13,15-19], exogenous stimuli (e.g., serum deprivation)[16,18] and "cell cycle blockers" (e.g., nocodazole)[13,15,18-20] for artificial synchronization of cell cycle, inevitably disturbed the cellular physiology and subsequent nanoparticle accumulation. Moreover, evaluation of nanoparticle accumulation with confocal laser scanning microscopy (CLSM) was limited at a two-dimensional (2D) level, in which spatial cellular architecture and heterogeneous intracellular distribution of nanoparticles were both ignored[13,17,19,20]. Indeed, these technical barriers have become "bottleneck" problems preventing deeper and further investigations in related research and development.

61 Autophagy is another major biological process involved in the maintenance of physiological
62 homeostasis and pathogenesis of a wide range of diseases[21]. Interestingly, recent studies indicate
63 that cancer cells are more dependent on autophagy than normal cells, with high levels of
64 endogenous autophagy detected in various types of cancers such as osteosarcoma and pancreatic
65 cancer[22,23]. Evolutionarily conserved autophagy-related genes (*ATG* genes) are core regulatory
66 genes of autophagy[21,24]. Moreover, endosomal/lysosomal system, which is critically involved in
67 nanoparticle accumulation[25], also plays a pivotal role in autophagy[26]. As a result, there is a growing
68 body of related reports, with the majority focusing on the possible capability of nanoparticles to
69 induce autophagy per se[27]. Up to date four literatures explored the potential effect of autophagy on
70 cellular accumulation of nanoparticles, including NIR-labelled carboxylated polystyrene
71 nanoparticles[28,29], C6 tagged Ag nanoparticles[30] and hyaluronic acid-modified MIL-125
72 nanoparticles loaded with doxorubicin-vitamin E succinate (HA-MIL125@DV) [31] all measured at
73 2D level. Considering that non-specific autophagy inhibitors were used to modulate autophagy in
74 these studies, the obtained data might be confounded by non-autophagy-related pharmacological
75 effects induced by these non-specific inhibitors[32].
76 This study was inspired by our strong curiosities on the impact of cell cycle and endogenous
77 autophagy on cellular accumulation of nanoparticles, and by the methodological challenges existed
78 in research on "nano-cell cycle/autophagy" interactions. Herein, a pair of isogenic cancer cell lines
79 including wild type (WT) strain and *ATG7* knockout (*ATG7* KO) derivative was applied to
80 eliminate the interferences caused by non-specific autophagy inhibitors. Importantly, by combining
81 transfection of cell cycle indicator plasmid PIP-FUCCI[33] and mitotic shake-off[34], an alive,
82 complete and thorough distinguishment of cells at four distinct cell cycle phases was successfully
83 achieved. Encouragingly, further integration with high-resolution CLSM and three-dimensional
84 (3D) reconstruction technique enabled multi-dimensional evaluations on cellular accumulation of
85 fluorescence-labelled nanoparticles. Through construction and application of this technical
86 platform, cellular accumulation of LIP of Doxil® and LNP of BNT162b2, two widely used
87 nanoparticles, at four distinct cell cycle phases and with specific autophagy status were parallelly
88 and systemically determined respectively. In addition, as a valuable technical solution for
89 simultaneously solving several methodological barriers, the correlations among parameters utilized
90 in the technical platform for determination of nanoparticle accumulation were evaluated.

Results

Synthesis and characterization of model nanoparticles DiD-LIP and DiD-LNP

Despite the wide application of LIP and LNP as drug carriers, our understandings on their "nano-bio" interactions are far from sufficient. So far, no literature has investigated the potential impact of either cell cycle or autophagy on the cellular accumulation of LIP or LNP. Hereby LIP and LNP were respectively synthesized according to officially published formulations[35,36] and our previous report[4], with DiD as a tracer fluorescence[37,38]. Briefly, DiD-LIP was formulated by hydrating a lipid mixture containing HSPC, cholesterol, $mPEG_{2000}$-DSPE and DiD in sucrose-histidine buffer, followed by downsizing using a 10-mL extruder barrel (Fig. 1a left). DiD-LNP was prepared with a microfluidic mixing device through mixing the ethanol phase containing ALC-0315, DSPC, cholesterol, ALC-159, DiD and the aqueous phase containing firefly luciferase mRNA to enhance the stability of LNP[4,39] (Fig. 1a right).

Further characterization with dynamic light scattering (DLS) showed that the Z-average/PDI of DiD-LIP and DiD-LNP were 104.433 ± 0.513 nm/0.102 ± 0.036 and 106.767 ± 0.306 nm/0.145 ± 0.009, respectively (Fig. 1b). Additional cryogenic transmission electron microscopy (Cryo-TEM) examination confirmed that DiD-LIP was characterized as hollow spheres, whereas DiD-LNP exhibited a typical electron-dense core structure containing mRNA (Fig. 1c, insert)[4]. Zeta potentials of DiD-LIP and DiD-LNP were -29.100 ± 2.081 mV and 3.660 ± 0.476 mV, respectively (Fig. 1c). These data demonstrate that both model nanoparticles possess highly monodisperse particle-size distribution and weak surface charge.

Importantly, DiD-LIP and DiD-LNP exhibited good stability when stored in phosphate buffer saline (PBS) at 4 °C, without remarkable changes detected for Z-average or PDI from Day 1 to Day 28 (Supplementary Fig. 1a-b; Supplementary Fig. 2), or in DMEM medium containing 10% fetal bovine serum (FBS) at 37 °C for up to 24 hours (simulating the experimental environment) (Fig. 1d-e; Supplementary Fig. 3). Both DiD-LIP and DiD-LNP displayed a single and size-stable intensity peak throughout the whole incubation period and under two distinct physiological conditions. Moreover, the standard curves of phospholipid and corresponding equations were obtained for further dosage determination of DiD-LIP and DiD-LNP (see "**Methods**", Supplementary Fig. 1c, d)[4].

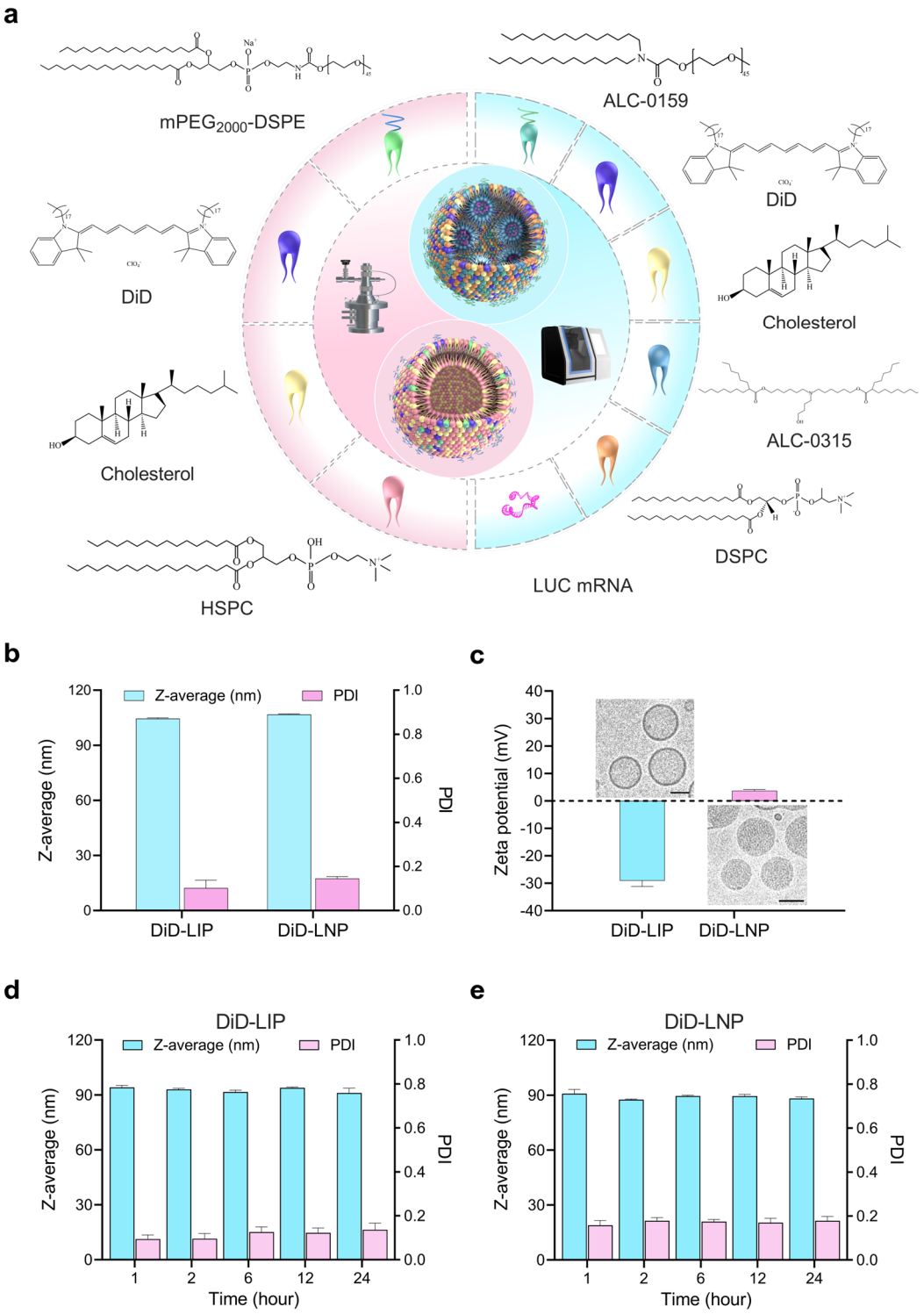

Fig. 1. Preparation and characterization of DiD-labelled liposomes (DiD-LIP) and lipid nanoparticles (DiD-LNP). a, Schematic illustration of the synthesis of DiD-LIP (left, pink background) and DiD-LNP (right, blue background). Briefly, to synthesis DiD-LIP, the sucrose-histidine buffer hydrated $mPEG_{2000}$-DSPE, DiD, cholesterol and HSPC to generate multilamellar vesicles, followed by size reduction through a 10-mL extruder barrel. To synthesize DiD-LNP, the ethanol phase dissolving ALC-0159, DiD, cholesterol, ALC-0315 and DSPC was mixed with the aqueous phase containing firefly luciferase mRNA (LUC mRNA) at a flow rate ratio of 1: 3 (ethanol: aqueous) via a microfluidic mixing device. **b-c**, Z-average, polydispersity index (PDI), Zeta potentials and representative Cryo-TEM images (inserts) of DiD-LIP and DiD-LNP. Scale bars, 50 nm. **d-e**, Z-average and

PDI of DiD-LIP and DiD-LNP in DMEM containing 10% FBS stored at 37 °C for up to 24 hours. Data in **b-e** were presented as "mean ± standard deviation" of three independent experiments. Z-average and PDI among various time points were evaluated by ANOVA with Bonferroni correction, with no statistically significant difference detected (all $P > 0.05$).

Establishment of a multi-functional technical platform for determining cell cycle- and autophagy-associated cellular accumulation of nanoparticles

Using empty vector as a control, the isogenic WT and *ATG7* KO U2OS cell lines previously constructed were transduced with lentiviral particles carrying the cell cycle-indicating PIP-FUCCI plasmid (see "**Methods**"). After screening with G418 and flow cytometry, corresponding WT and *ATG7* KO PIP-FUCCI cell lines expressing strong mVenus (green fluorescence) and/or mCherry (red fluorescence) were obtained (Fig. 2a). PIP-FUCCI transfection and subsequent selection had marginal influence on cellular morphology and proliferation rate (Supplementary Figs. 4 and 5).

However, although single positivity of mVenus and mCherry could respectively indicate cells at G1-phase and S-phase, both G2-phase and M-phase cells are mVenus and mCherry double-positive and exhibit yellow fluorescence (overlap of green and red). That is, PIP-FUCCI transfection by itself cannot distinguish between G2-phase and M-phase cells in situ. Fortunately, different from G1-phase, S-phase and G2-phase cells naturally adhering to the culture dish with polyhedral shapes, typical M-phase cells have unique properties such as spherical shape[40] and significantly reduced adhesion capability or suspended state in culture media due to "mitotic rounding", leading to convenient collection of M-phase cells through gentle mitotic shake-off[34]. Enlightened by these characteristics, we combined PIP-FUCCI transfection with mitotic shake-off, through which an approach thoroughly distinguishing four cell cycle phases was established. In addition, labelling cell membrane with FITC-EpCAM prior to mitotic shake-off helped to exclude apoptotic cells and cellular debris via drawing the outline of cell membrane (see "**Methods**"; Fig. 2b, highlighted with dashed frame).

Further integration of high-resolution CLSM and 3D reconstruction technique significantly strengthened this multi-functional platform for determining cell cycle- and autophagy-associated cellular accumulation of nanoparticles (Fig. 2b). Using DiD-LIP (blue fluorescence) as a representative, nanoparticle accumulation was not only characterized at different dimensional levels, but respectively evaluated at four distinct cell cycle phases in WT and *ATG7* KO PIP-

159 FUCCI cells (Fig. 2c). In brief, this new platform has multiple superiorities including complete and
160 thorough separation and collection of alive cells at four cell cycle phases, elimination of
161 interferences caused by "extra" treatments (e.g. cell dissociation agents, cell cycle synchronization
162 drugs, none-specific autophagy inhibitors), and capability for parallel investigations on multiple
163 biological parameters/dimensions.

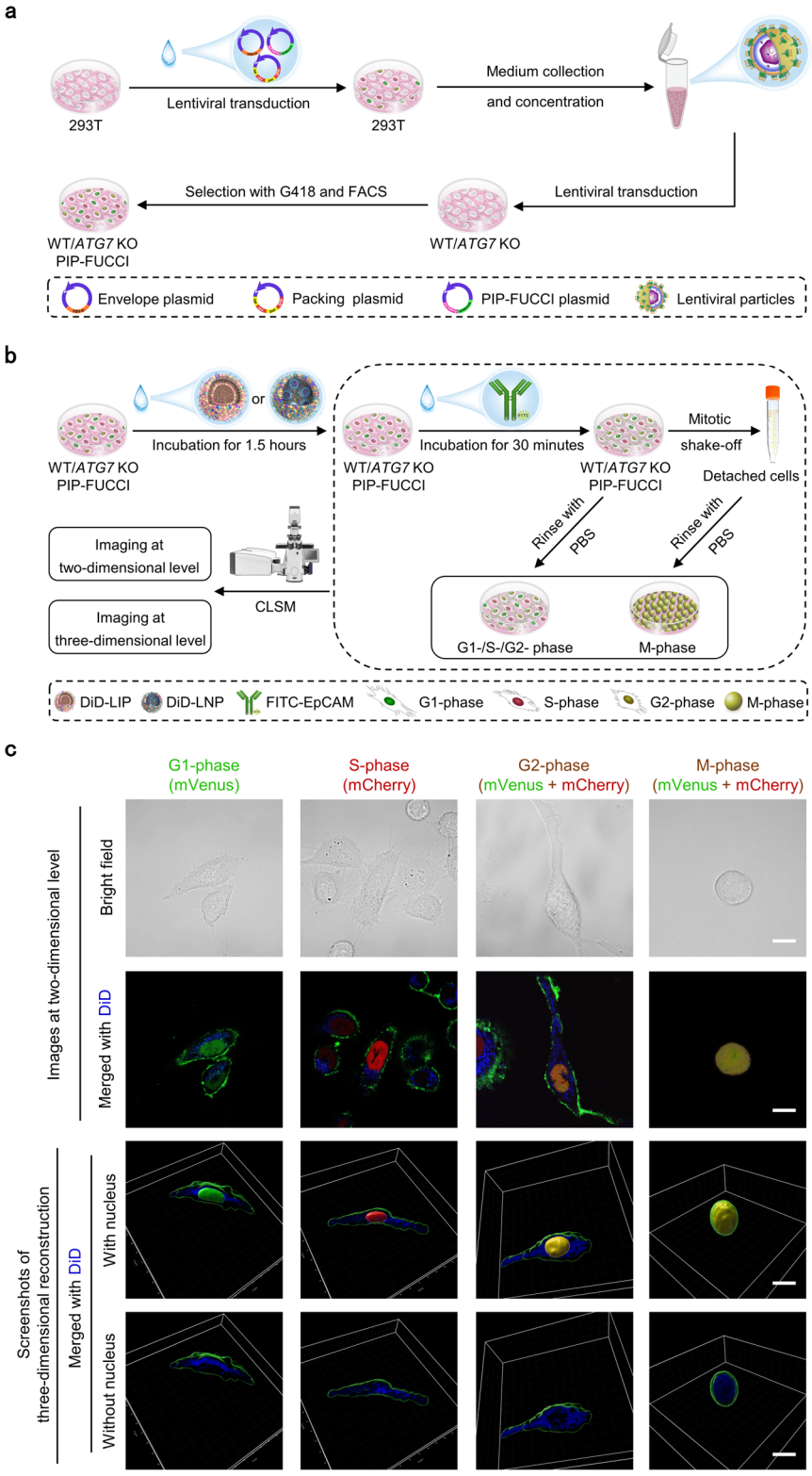

164 **Fig. 2. Establishment of an alive and multi-functional technical platform for determining cell cycle- and**
165 **autophagy-associated nanoparticle accumulation. a,** Schematic diagram shows the construction of cell lines
166 stably expressing PIP-FUCCI (cell cycle indicator) plasmid. Envelope plasmid PMD2.G, packing plasmid
167 psPAX2 and transfer plasmid PIP-FUCCI were simultaneously added into 293T cells. Afterwards, the culture
168 medium was collected and concentrated, followed by application of lentiviral supernatant containing PIP-FUCCI
169 to isogenic wide type (WT) and *ATG7* knockout (*ATG7* KO) U2OS cell lines. Subsequently, WT and *ATG7* KO
170 PIP-FUCCI cell lines stably expressing PIP-FUCCI were obtained after selection with G418 and flow cytometry
171 (FACS). **b**, Schematic diagram indicates the establishment of a multi-functional platform for determining cell
172 cycle phase- and autophagy-associated nanoparticle accumulation. WT and *ATG7* KO PIP-FUCCI cells were
173 treated with DiD-labelled liposomes (DiD-LIP, equivalent to 5 μg/mL DOX) or lipid nanoparticles (DiD-LNP,
174 equivalent to 6 μg/mL luciferase mRNA) for 1.5 hours, followed by FITC-EpCAM incubation for 30 minutes to
175 label cell membrane (green cell membrane). Complete distinguishment and collection of cells at four distinct cell
176 cycle phases was achieved through combining PIP-FUCCI expression to indicate G1-phase (mVenus positive,
177 green nucleus), S-phase (mCherry positive, red nucleus) and G2-phase (mVenus and mCherry double-positive,
178 yellow nucleus) cells attached to culture dish, with mitotic shake-off to collect detached or floating M-phase cells
179 (mVenus and mCherry double-positive, yellow nucleus). Further integration of confocal laser scanning
180 microscope (CLSM) and three-dimensional reconstruction technique enabled detection and calculation of
181 nanoparticle accumulation at both two-dimensional and three-dimensional levels. **c**, Representative light
182 microscopic and CLSM images demonstrating the successful construction and application of new technical
183 platform, using DiD-LIP (blue fluorescence) and WT PIP-FUCCI cells as a model system. Scale bars, 20 μm.
184

185 It is noteworthy that although cells harvested with mitotic shake-off have been described as
186 all M-phase cells[41], a rare population of just divided spherical daughter cells having not fully re-
187 adhered to the dish might be simultaneously collected. However, daughter cells just completed
188 mitosis have actually entered a new cell cycle and are at G1-phase. Due to rapid decay of mCherry
189 protein, daughter cells quickly become mVenus single-positive displaying green nuclear
190 fluorescence, which differs from the pre-division mitotic cells with yellow nuclear fluorescence[33].
191 Therefore, suspended daughter cells will neither be selected nor analyzed as M-phase cells by
192 mistake in this study.

193 To further confirm these characteristics, routinely cultured WT and *ATG7* KO PIP-FUCCI
194 cells without exposure to nanoparticles were monitored with CLSM for up to 25 hours (estimated
195 cell doubling time, Supplementary Fig. 6). Using individually tracked cancer cells as examples,
196 our "longitudinal" data further demonstrated the reliability of combining PIP-FUCCI expression
197 with morphological examination for precise cell cycle indication throughout a complete cell cycle
198 including "M-to-G1" phase transition (Supplementary Fig. 6). Moreover, our findings indicating

199 gradual increases in cell volume while cell cycle progression have provided another piece of
200 evidence that the M-phase cells analyzed herein were pre-division mother cells with maximum cell
201 volumes, but not just divided daughter cells minimum cell volumes (see subsequent "**Results**").
202

203 **Little influence of DiD-LIP and DiD-LNP per se on cell cycle distribution and autophagy of**
204 **WT and *ATG7* KO PIP-FUCCI cell lines**

205 To clarify the impact of cell cycle and autophagy on nanoparticle accumulation, the possible
206 interference of model nanoparticles on cancer cells per se needs to be firstly excluded. Therefore,
207 WT and *ATG7* KO PIP-FUCCI cells were respectively treated with DiD-LIP and DiD-LNP for
208 further evaluation. As depicted in Fig. 3a and Supplementary Table 1, flow cytometry analysis
209 showed that percentages of nanoparticle-untreated cancer cells at G1-phase, S-phase, G2-phase and
210 M-phase were 33.10 ± 1.77%, 54.83 ± 2.82%, 11.81 ± 0.93% and 0.26 ± 0.19%, respectively, for
211 WT PIP-FUCCI cell line, and 31.30 ± 2.21%, 54.22 ± 2.49%, 13.94 ± 1.29% and 0.53 ± 0.16%,
212 respectively, for *ATG7* KO PIP-FUCCI cell line. Percentages of DiD-LIP-treated WT and *ATG7*
213 KO PIP-FUCCI cell lines at G1-phase, S-phase, G2-phase and M-phase were 33.18 ± 2.08%, 54.64
214 ± 3.14%, 11.92 ± 1.09% and 0.26 ± 0.17%, respectively, and 31.25 ± 2.15%, 53.99 ± 2.37%, 14.29
215 ± 0.57%, 0.48 ± 0.10%, respectively. Correspondingly, the cell cycle distributions of DiD-LNP-
216 treated WT and *ATG7* KO PIP-FUCCI cell lines at G1-phase, S-phase, G2-phase and M-phase
217 were 33.70 ± 2.36%, 54.38 ± 3.37%, 11.66 ± 0.92% and 0.27 ± 0.21%, respectively, and 31.15 ±
218 0.61%, 55.02 ± 1.58%, 13.27 ± 1.44% and 0.56 ± 0.16%, respectively. Importantly, further
219 statistical analysis demonstrated that no matter with or without nanoparticle treatment, no
220 significant difference on cell cycle distribution was observed in WT and *ATG7* KO PIP-FUCCI
221 cells (Supplementary Table 2).

222 Moreover, data obtained with additional regular flow cytometry assay (without mitotic shake-
223 off) at longer time points demonstrated that in both WT and *ATG7* KO PIP-FUCCI cell lines,
224 neither DiD-LIP nor DiD-LNP exhibited significant influence on general cell cycle distribution
225 after administration for 12 hours, 24 hours and 48 hours, respectively (Supplementary Figs. 7 and
226 8, Supplementary Table 3 and Table 4).

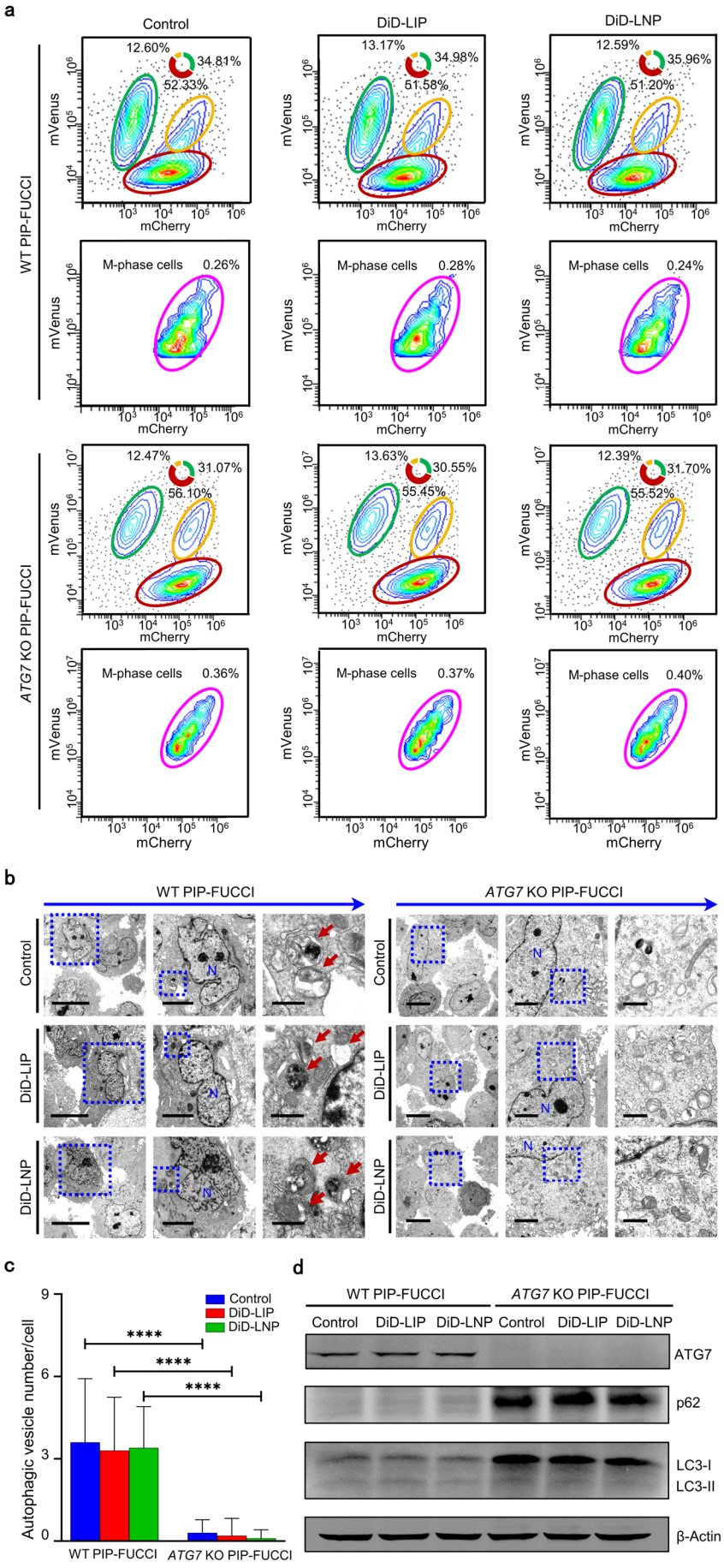
a
Control
DiD-LIP
DiD-LNP
WT PIP-FUCCI
ATG7 KO PIP-FUCCI
mVenus
mCherry
12.60%
34.81%
52.33%
13.17%
34.98%
51.58%
12.59%
35.96%
51.20%
M-phase cells 0.26%
M-phase cells 0.28%
M-phase cells 0.24%
12.47%
31.07%
56.10%
13.63%
30.55%
55.45%
12.39%
31.70%
55.52%
M-phase cells 0.36%
M-phase cells 0.37%
M-phase cells 0.40%
b
WT PIP-FUCCI
ATG7 KO PIP-FUCCI
Control
DiD-LIP
DiD-LNP
N
c
Autophagic vesicle number/cell
Control
DiD-LIP
DiD-LNP
****
WT PIP-FUCCI
ATG7 KO PIP-FUCCI
d
WT PIP-FUCCI
ATG7 KO PIP-FUCCI
Control
DiD-LIP
DiD-LNP
ATG7
p62
LC3-I
LC3-II
β-Actin

227

228 **Fig. 3. Validation of cell cycle distribution and endogenous autophagy in WT and *ATG7* KO PIP-FUCCI**
229 **cells with or without nanoparticle treatment. a**, Representative flow cytometry data on thorough cell cycle
230 distribution. Cells accumulated at G1-phase, S-phase and G2-phase (upper panel for each cell line), as well as
231 M-phase (isolated with mitotic shake-off; lower panel for each cell line) were respectively circled in green, red,
232 orange and purple, with corresponding percentages indicated. **b**, Representative transmission electron microscope
233 images of autophagic vesicles indicated by rust-red arrows. N, nucleus. Scale bars, from left to right, 10 μm, 4
234 μm and 1 μm for WT PIP-FUCCI cells, and 10 μm, 3 μm and 1 μm for *ATG7* KO PIP-FUCCI cells. **c**, Statistical
235 analysis of the autophagic vesicle number per cell. Data were presented as "mean ± standard deviation" (n = 10)
236 and further analyzed by Mann-Whitney U test. ****, $P < 0.0001$. **d**, Representative western blot analysis of
237 autophagy-related proteins including ATG7, p62 and LC3. WT PIP-FUCCI, wide type U2OS cells stably
238 expressing PIP-FUCCI; *ATG7* KO PIP-FUCCI, *ATG7* knockout U2OS cells stably expressing PIP-FUCCI. DiD-
239 labelled liposomes (DiD-LIP) and lipid nanoparticles (DiD-LNP) were administered to cancer cells at a dose
240 equivalent to 5 μg/mL DOX and a dose equivalent to 6 μg/mL luciferase mRNA, respectively for 2 hours.
241
242 Previous studies demonstrate that *ATG7* knockdown effectively blocked cellular autophagy[42].
243 Indeed, although autophagic vesicles (AVs, including autophagosomes and autophagic lysosomes)
244 with typical double-layer membrane structure were easily observed in WT PIP-FUCCI cells with
245 TEM, no typical AVs were seen in *ATG7* KO PIP-FUCCI cells (Fig. 3b). Further statistical analysis
246 confirmed significantly fewer AVs in *ATG7* KO PIP-FUCCI cells than in WT PIP-FUCCI cells
247 (Fig. 3c; Supplementary Table 5). As anticipated, ATG7 protein level was high in WT PIP-FUCCI
248 cells while undetectable in *ATG7* KO PIP-FUCCI cells in Western blotting (Fig. 3d). Moreover,
249 LC3-II/LC3-I ratio, which is positively correlated with the autophagy level[43], was significantly
250 decreased in *ATG7* KO PIP-FUCCI cells. In contrast, p62, which is negatively correlated with
251 autophagy[43], was dramatically increased in *ATG7* KO PIP-FUCCI cells. Our data firmly
252 demonstrated the successful blockade of autophagy in *ATG7* KO PIP-FUCCI cells. Encouragingly,
253 neither DiD-LIP nor DiD-LNP exhibited any effect in aforementioned assays, indicating that
254 designated nanoparticle treatment had marginal impact on the autophagy of WT and *ATG7* KO
255 PIP-FUCCI cells.
256
257 **Determination of cell cycle- and endogenous autophagy-associated cellular accumulation of**
258 **DiD-LIP**
259 Next, we meticulously captured abundant CLSM images with intracellular co-localization of cell
260 cycle-indicating fluorescence and DiD-LIP using this new platform (Supplementary Videos 1-8;

261 Supplementary Fig. 9). Subsequently, cell size, Total Fluorescence Intensity (TFI) and Mean
262 Fluorescence Intensity (MFI) were respectively calculated and analyzed at 2D and 3D levels (Fig.
263 4; Table 1; Supplementary Tables 6 and 7). Our data showed that TFI (2D) of DiD-LIP across
264 various cell cycle phases exhibited same characteristics in both cell lines, which was M < G1 ≈ S
265 < G2. Further integration of 3D reconstruction technique revealed the following cell cycle-
266 associated characteristics of TFI (3D) of DiD-LIP: M (≈ G1) < (G1 ≈) S < G2 in WT PIP-FUCCI
267 cells; M < G1 < S < G2 in *ATG7* KO PIP-FUCCI cells.

268 As expected, both cell lines exhibited a gradual increase in cell area (2D level) upon cell cycle
269 progressing from G1-phase to G2-phase, followed by a decrease at M-phase due to "mitotic
270 rounding" to become spherical[44]. Consistent with previous reports, cell volume (3D level) gradually
271 increased while cells sequentially going through G1-phase, S-phase, G2-phase and M-phase of the
272 cell cycle[45,46]. Furthermore, MFI (2D) based on cell area and MFI (3D) based on cell volume were
273 initially calculated and analyzed. Impressively, MFI (2D) and MFI (3D) of DiD-LIP exhibited same
274 cell cycle-associated characteristics in both cell lines, which was M < G1 ≈ S ≈ G2. These data
275 may suggest that the relatively higher increase in cell size of G2-phase cells attenuated the
276 aforementioned difference in TFI detected between G2-phase and G1-phase/S-phase. Taken
277 together, our study not only differentiated between G2-phase and M-phase cells in physiological
278 state, but provided initial evidence that cells at G2-phase and M-phase respectively had the
279 maximum and minimum nanoparticle accumulation. Interestingly, it has been suggested that M-
280 phase cells have declined endocytosis and elevated cell membrane tension, which may assist
281 mother cell to prevent external disturbances during mitosis[47]. These properties support our findings
282 that M-phase cells had minimum nanoparticle accumulation among four cell cycle phases.

283 As mentioned above, discrepant results were reported in literatures investigating the influence
284 of cell cycle on nanoparticle accumulation[13-20]. For instance, although accumulation of CdTe
285 QDs[13,14], ZnO[15], PS-CCOH[16] and FITC–dextran fibroin-encapsulated microspheres[17] showed same
286 cell cycle-associated characteristics (G2/M > S > G1), FITC@NPs-cRGD accumulation exhibited
287 a reverse ranking (G1 > S > G2/M). It should be noted that cells at G2-phase and M-phase were
288 muddled up as G2/M-phase cells in most previous studies[13-19], except G2-phase and M-phase
289 synchronizations were respectively induced using RO3306 and paclitaxel in a study investigating
290 cell-cycle-dependent macropinocytosis of Tat/pDNA-Ca^{2+} nanoparticles[20].

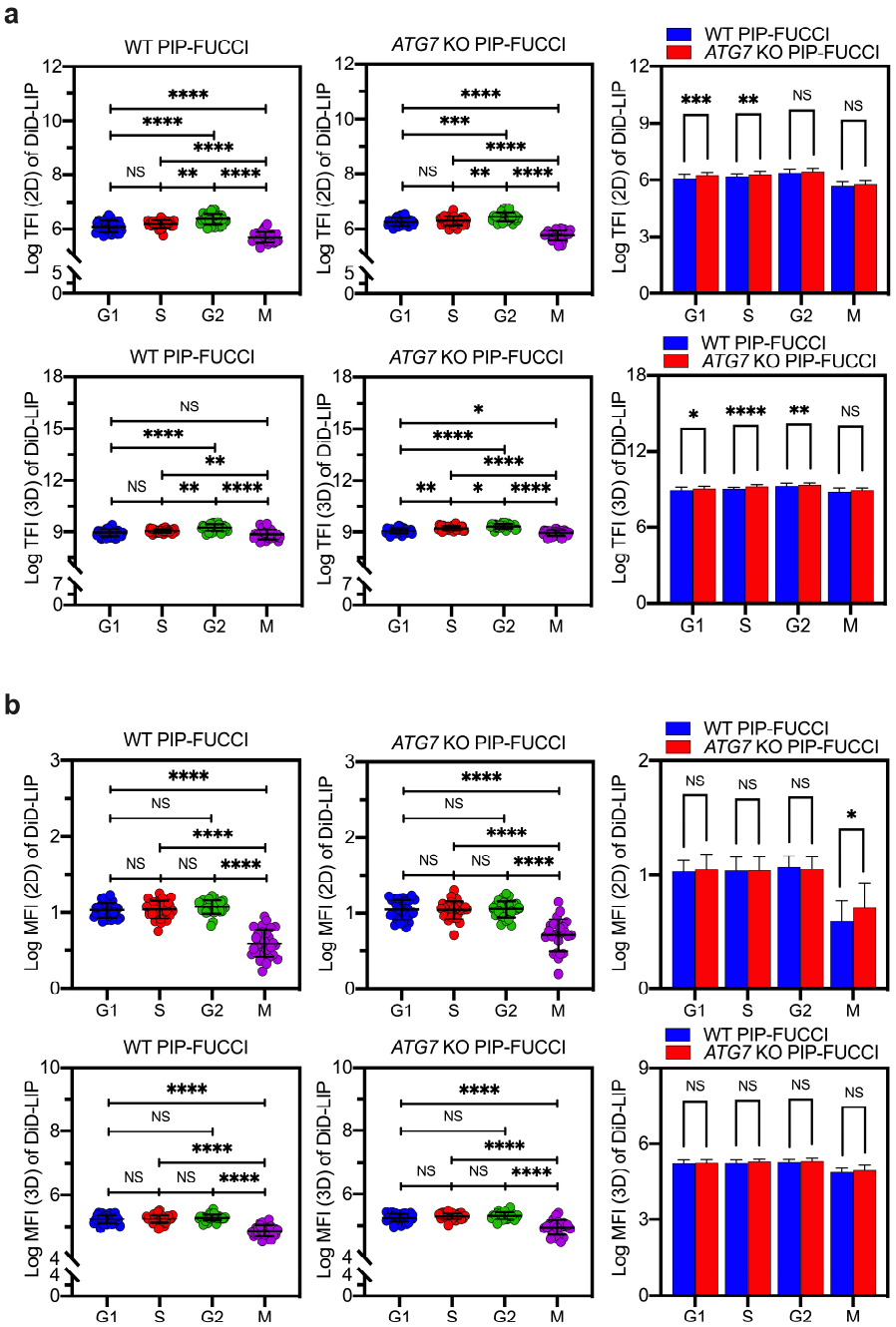

Fig. 4. Determination of cell cycle- and endogenous autophagy-associated cellular accumulation of DiD-labelled liposomes (DiD-LIP) using the newly established technical platform. a, Statistical analysis of Total Fluorescence Intensity (TFI) in G1-phase, S-phase, G2-phase and M-phase WT and *ATG7* KO PIP-FUCCI cells respectively measured at two-dimensional (2D, upper panel) and three-dimensional (3D, lower panel) levels. **b**, Statistical analysis of Mean Fluorescence Intensity (MFI) in WT and *ATG7* KO PIP-FUCCI cells respectively measured at aforementioned four cell cycle phases, as well as at 2D (upper panel) and 3D (lower panel) levels. WT PIP-FUCCI, wide type U2OS cells stably expressing PIP-FUCCI; *ATG7* KO PIP-FUCCI, *ATG7* knockout U2OS cells stably expressing PIP-FUCCI. DiD-LIP was administered at a dose equivalent to 5 μg/mL DOX for 2 hours. All data were analyzed after $\log_{10}$ transformation and presented as "mean ± standard deviation" (n = 25-30). Statistical analysis of DiD-LIP accumulation among four distinct cell cycle phases was conducted using ANOVA with Bonferroni correction, while differences between WT and *ATG7* KO PIP-FUCCI cell lines were

evaluated with an independent sample *t*-test. *, $P < 0.05$; **, $P < 0.01$; ***, $P < 0.001$; ****, $P < 0.0001$. NS, not significant.

Moreover, both TFI and MFI of DiD-LIP suggested an association between nanoparticle accumulation and endogenous autophagy. For instance, TFI (2D) of G1-phase and S-phase *ATG7* KO PIP-FUCCI cells, TFI (3D) of G1-phase, S-phase and G2-phase *ATG7* KO PIP-FUCCI cells, as well as MFI (2D) of M-phase *ATG7* KO PIP-FUCCI cells, all exhibited significant increases and surpassed those of WT PIP-FUCCI cells. Previously there are four literatures explored the influence of autophagy on nanoparticle accumulation, all of which using 2D fluorescence intensity for accumulation assessment and non-specific autophagy inhibitors for autophagy inhibition. Among these reports, Fageria et al. reported a reduced cellular accumulation of Ag nanoparticles upon chloroquine treatment[30], and Sipos et al. observed a suppressed cellular accumulation of polystyrene nanoparticles after exposure to 3-methyladenine and bafilomycin A1[28,29]. However, interestingly, co-loading of 3-methyladenine into HA-MIL125@DV nanoparticles (so called HA-MIL125@DVMA) led to significantly increased nanoparticle accumulation in both drug-sensitive MCF-7 and multidrug-resistant MCF-7/ADR cell lines[31]. Although multiple contributing factors such as nanoparticle- and/or cell line-specificity might be involved in mediating the different findings, it is noteworthy that different from *ATG7* knockout that specifically blocks endogenous autophagy, non-autophagy-related pharmacological effects such as induction of cell death and lysosomotropic activities have been reported for chloroquine, 3-methyladenine and bafilomycin A1, which may interfere with the cellular accumulation of nanoparticles[48,49].

Determination of cell cycle- and endogenous autophagy-associated cellular accumulation of DiD-LNP

WT and *ATG7* KO PIP-FUCCI cells were further treated with DiD-LNP and evaluated with the multi-functional platform (Fig. 5; Table 1; Supplementary Videos 9-16; Supplementary Fig. 10; Supplementary Tables 8 and 9). Impressively, TFI (2D) of DiD-LNP in both cell lines, and TFI (3D) and MFI (2D) of DiD-LNP in WT PIP-FUCCI cell line, all exhibited same cell cycle-associated characteristics as TFI (2D) of DiD-LIP, which was M < G1 ≈ S < G2. MFI (3D) in WT and TFI (3D) in *ATG7* KO PIP-FUCCI cells showed similar characteristics, except G1 < S in WT and M ≈ G1 in *ATG7* KO PIP-FUCCI cells. Moreover, MFI (2D) and MFI (3D) in *ATG7* KO

333 PIP-FUCCI cells were M < G1 ≈ S ≈ G2 and M < (G1 ≈) S < (G1 ≈) G2, respectively, coinciding
334 with the aforementioned attenuation of differences between G2-phase and G1-phase/S-phase due
335 to relatively higher increase in cell size of G2-phase cells. In general, multi-dimensional data
336 obtained with DiD-LNP confirmed that G2-phase cells had maximum whereas M-phase cells had
337 minimum nanoparticle accumulation. Interestingly, we noted that mean values of TFI and MFI of
338 two model nanoparticles exhibited similar tendency in both cell lines, which is M < G1 < S < G2.
339 These data might imply that when proliferating cells progress into a new cell cycle with
340 physiological activities such as cellular protein and DNA synthesis gradually intensifying,
341 nanoparticle accumulation becomes active in synchronization till the cells enter "torpid" M-
342 phase[50,51].

343 Moreover, it is noteworthy that M-phase cells have the minimum cell areas, which would
344 weaken the difference of MFI (2D) between M-phase cells and cells at other phases. Nevertheless,
345 M-phase cells of both cell lines still exhibited extremely significant decrease in MFI (2D) upon
346 treatment with two model nanoparticles (nearly all $P < 0.0001$). In contrast, M-phase cells have the
347 maximum cell volumes, which would strengthen the difference of MFI (3D) between M-phase cells
348 and cells at other phases. It is thereby logical that the following significant differences in MFI (3D)
349 arose, although no difference was detected with corresponding TFI (3D): M < G1 in MFI (3D) of
350 DiD-LIP in WT PIP-FUCCI cells, M < G1 and M < S in MFI (3D) of DiD-LNP in *ATG7* KO PIP-
351 FUCCI cells, all $P < 0.0001$.

352 Interestingly, different from DiD-LIP that exhibited several significantly higher TFI and MFI
353 in *ATG7* KO PIP-FUCCI cells than those in WT PIP-FUCCI cells, DiD-LNP showed increased
354 TFI but reduced MFI in *ATG7* KO PIP-FUCCI cells compared with WT strain. In detail, TFI (2D)
355 of M-phase, and TFI (3D) of G1-phase and M-phase *ATG7* KO PIP-FUCCI cells were significantly
356 higher than those of WT PIP-FUCCI cells. However, both MFI (2D) and MFI (3D) of S-phase and
357 G2-phase *ATG7* KO PIP-FUCCI cells were significantly lower than those in WT strain. These data
358 indicate that autophagy might have diverse influences on cellular accumulation of nanoparticles
359 which deserves further investigation. Moreover, although cellular accumulation of DiD-LIP and
360 DiD-LNP exhibited several common characteristics, varied features were also observed between
361 these two nanoparticles regarding cell cycle- and autophagy-associated cellular accumulation.
362 These variations might attribute to different physiochemical properties between DiD-LIP and DiD-

363 LNP, e.g. surface charge, nanoparticle composition and spatial structure, leading to distinctive
364 "nano-bio" interactions such as different characteristics in endocytosis, subsequent endo-lysosomal
365 escape, degradation and even exocytosis of nanoparticles.

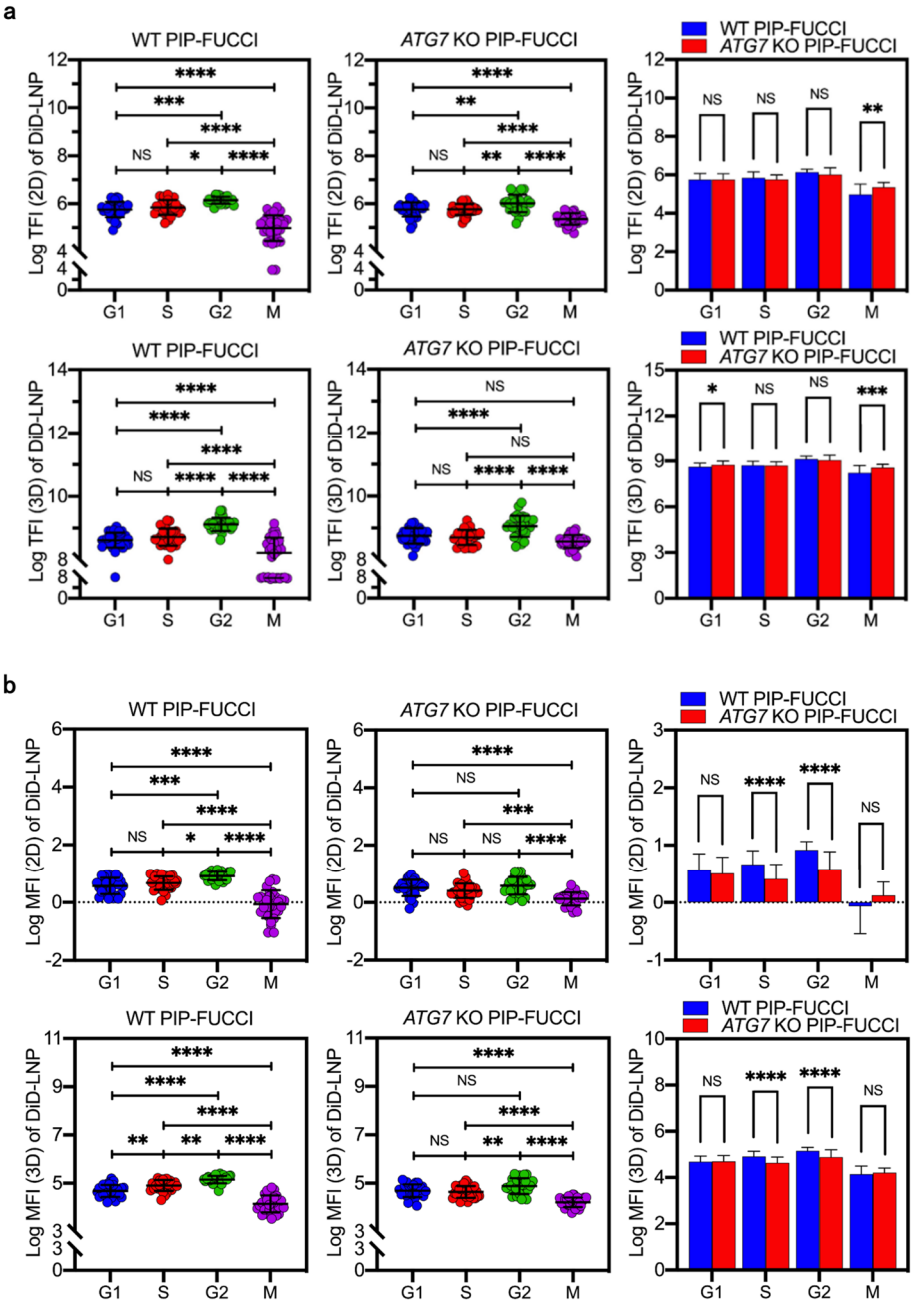

366

367 **Fig. 5. Determination of cell cycle- and endogenous autophagy-associated cellular accumulation of DiD-**
368 **labelled lipid nanoparticles (DiD-LNP) using the newly established technical platform. a**, Statistical analysis
369 of Total Fluorescence Intensity (TFI) in G1-phase, S-phase, G2-phase and M-phase WT and *ATG7* KO PIP-
370 FUCCI cells respectively measured at two-dimensional (2D, upper panel) and three-dimensional (3D, lower panel)
371 levels. **b**, Statistical analysis of Mean Fluorescence Intensity (MFI) in WT and *ATG7* KO PIP-FUCCI cells
372 respectively measured at four distinct cell cycle phases, as well as at 2D (upper panel) and 3D (lower panel)
373 levels. WT PIP-FUCCI, wide type U2OS cells stably expressing PIP-FUCCI; *ATG7* KO PIP-FUCCI, *ATG7*

knockout U2OS cells stably expressing PIP-FUCCI. DiD-LNP was administered at a dose equivalent to 6 μg/mL luciferase mRNA for 2 hours. All data were analyzed after $\log_{10}$ transformation and presented as "mean ± standard deviation" (n = 25-30). Statistical analysis of DiD-LIP accumulation among four distinct cell cycle phases was conducted using ANOVA with Bonferroni correction, while differences between WT and *ATG7* KO PIP-FUCCI cell lines were evaluated with an independent sample *t*-test. *, $P < 0.05$; **, $P < 0.01$; ***, $P < 0.001$; ****, $P < 0.0001$. NS, not significant.

Characterization of fluorescence intensity-based parameters utilized in determination of cellular accumulation of DiD-LIP and DiD-LNP

Considering that TFI (2D), TFI (3D), MFI (2D) and MFI (3D) were firstly used in combination for determination of nanoparticle accumulation, their correlations were assessed with Spearman or Pearson Correlation Coefficients (see "Methods"). As indicated in Table 2, when the correlations between two dimensional levels were respectively evaluated for TFI and MFI in WT and *ATG7* KO PIP-FUCCI cells, moderate to very high Correlation Coefficients were obtained for all the assessed groups. Nevertheless, moderate to high Correlation Coefficients ($r = 0.689 \sim 0.793$, all $P < 0.0001$) were achieved for TFI and MFI of DiD-LIP, while high to very high correlations ($r = 0.811 \sim 0.932$, all $P < 0.0001$) were detected for those of DiD-LNP. Interestingly, further correlation analysis between TFI and corresponding MFI at same dimensional level revealed low to high Correlation Coefficients ($r = 0.495 \sim 0.711$, all $P < 0.0001$) for TFI and MFI of DiD-LIP, but high to very high Correlation Coefficients ($r = 0.791 \sim 0.918$, all $P < 0.0001$) for those of DiD-LNP ($r = 0.791$, $P < 0.0001$) (Table 3).

Importantly, further Statistical analysis using z-test on Fisher z-transformed correlation coefficients discovered that there were statistical significances between different nanoparticles and different cell lines on aforementioned Correlation Coefficients among TFI and MFI. For instance, Correlation Coefficients among TFI and MFI in DiD-LIP-treated groups were significantly lower than those treated with DiD-LNP in WT and *ATG7* KO PIP-FUCCI cells (*P* values, 0.0441 ~ < 0.0001), except no correlation detected between TFI (2D) and TFI (3D) of DiD-LIP with that of DiD-LNP in *ATG7* KO PIP-FUCCI cells ($P = 0.0860$) (Supplementary Table 10). In addition, when comparing Correlation Coefficients among TFI and MFI in different cell lines, Correlation Coefficient between MFI (2D) and TFI (2D) of DiD-LNP in WT PIP-FUCCI cells was significantly higher than that in *ATG7* KO PIP-FUCCI cells ($P = 0.0275$) (Supplementary Table 11). These data suggest that nanoparticle type and *ATG7* expression status, particularly the former, may affect the

correlation strength among fluorescence intensity-based parameters for nanoparticle accumulation determination.

On the other hand, as cell volumes gradually "grow" while cell cycle progressing, we further evaluated whether the increased fluorescence intensities were associated with increased cell volumes rather than cell cycle phases. Surprisingly, using TFI (3D) of DiD-LIP and DiD-LNP in WT and *ATG7* PIP-FUCCI cells as representative models, remarkable variations on Pearson Correlation Coefficients between TFI (3D) and cell volume were obtained among distinct cell cycle phases, as well as between different nanoparticles and cell lines (Supplementary Fig. 11 and Fig. 12). For instance, no correlation between TFI (3D) and cell volume was detected in the following groups: DiD-LIP-treated M-phase *ATG7* KO PIP-FUCCI cells, DiD-LNP-treated G1-phase WT PIP-FUCCI cells, as well as DiD-LNP-treated G1-phase, S-phase and G2-phase *ATG7* KO PIP-FUCCI cells, all $P > 0.05$. However, high Correlation Coefficients between TFI (3D) of DiD-LIP and cell volumes were achieved in WT PIP-FUCCI cells at of G1-phase ($r = 0.808$), G2-phase ($r = 0.860$) and M-phase ($r = 0.805$), while a low correlation coefficient ($r = 0.493$) was detected in S-phase WT PIP-FUCCI cells. Taken together, our data did not provide sufficient evidences on a clear correlation between fluorescence intensity-based parameters and cell sizes.

Discussion

This study aims to evaluate the impact of cell cycle and endogenous autophagy on cellular accumulation of nanoparticles under conditions largely mimicking physiological status. Through construction and application of a platform simultaneously overcoming several long-lasting methodological obstacles, we present initial and multi-dimensional data demonstrating that G2-phase and M-phase cells respectively have the maximum and minimum accumulation of DiD-LIP and DiD-LNP (Fig. 4 and Fig. 5; Table 1). Nevertheless, these two distinct cell populations were previously muddled up together (so called G2/M-phase cells) because of methodological deficiencies in distinguishing one population from another without scathe. Moreover, differential accumulation of DiD-LIP and DiD-LNP was not only observed between spherical M-phase and adherent G2-phase cells, but also occurred among adherent cells in both WT and *ATG7* KO PIP-FUCCI cells. Interestingly, among adherent cells at three distinct cell cycle phases, mean values of TFI and MFI of both nanoparticles exhibited similar tendency in WT and *ATG7* KO PIP-FUCCI

436 cells, which was G1 < S < G2. These findings may suggest a synchronization in intensified cellular
437 metabolism and enhanced nanoparticle accumulation while cell cycle progressing from G1-phase
438 to G2-phase. However, detailed mechanisms mediating cell cycle-associated nanoparticle
439 accumulation warrant further explorations, particularly for "torpid" M-phase cells. On the other
440 hand, our findings generally suggest an enhanced nanoparticle accumulation medicated by *ATG7*
441 knockout, as demonstrated by TFI/MFI of LIP and TFI of LNP. Although further verification and
442 exploration on underlying mechanisms are needed, our data may provide a novel line of supportive
443 evidence for combined use of anticancer modalities with autophagy blockers currently under
444 preclinical and clinical evaluations[52,53].

445 It is noteworthy that in this cross-sectional study, cells representative for distinct cell cycle
446 phases were randomly selected based on nuclear fluorescence and microscopic morphology.
447 However, durations for each cell cycle phase have significant variations among different cell types
448 and even within the same cell type cultured in different conditions. These variations are more
449 pronounced in cancer cells due to their well-known heterogeneity. According to the known phase
450 durations for mammalian cells and 2 hour-incubation timepoint designated, the representative cells
451 selected in our study may include a majority of cells remaining in the same phase throughout the
452 incubation period and a small portion progressed from the previous phase, particularly for G1-
453 phase, S-phase and G2-phase cells. As this study intends to determine the intracellular nanoparticle
454 levels for cells at four distinct cell cycle phases and with specific autophagy status respectively at
455 the time of analysis, the net value added during each cell cycle phase has not been investigated
456 herein. Nevertheless, acquiring time-lapse live cell imaging could help elucidating this interesting
457 issue. Indeed, our preliminary longitudinal experiment conducted in WT and *ATG7* KO PIP-
458 FUCCI cells monitored with CLSM for up to 25 hours has provided useful information and laid
459 the foundation for further exploration on this topic (Supplementary Fig. 6).

460 A technical detail worth mentioning is that although the distinction between routinely growing
461 adherent G2-phase and spherical M-phase cells based on morphology and attachment is
462 straightforward in microscopy, in the present study, cultured cancer cells were firstly administered
463 with fluorescence-labelled nanoparticles and EpCAM antibody. Afterwards, culture dishes
464 underwent gentle rinses with PBS to remove unbounded nanoparticles and antibody. As suspended
465 cells in culture medium will be directly removed with PBS rinses, mitotic shake-off was adopted

466 to separately harvest mitotic cells. Subsequently, settled and concentrated mitotic cells were
467 transferred to another culture dish after gentle rinses for image acquisitions, in parallel with
468 adherent cells maintained in original culture dish (Fig. 2). In combination with cell cycle indicator
469 PIP-FUCCI, this approach not only achieved thorough distinguishment of cells at four distinct cell
470 cycle phases with minimal disturbance in physiological state, but enabled us to obtain a favorable
471 number of mitotic cells. Meanwhile, increased efficiency and higher quality were achieved for
472 time-sensitive image acquisition and 3D reconstruction with CLSM, as no interference existed
473 among adherent and suspended cells.

474 To attenuate the potential influence of cell shape (particularly between cells at M-phase and
475 other phases) and cell size, nanoparticle accumulation was determined at multi-dimensional levels,
476 with TFI and MFI at both 2D and 3D levels were respectively calculated. Undoubtedly, integration
477 of TFI (2D), TFI (3D), MFI (2D) and MFI (3D), four fluorescence intensity-based and correlated
478 parameters as assessed with Spearman Correlation Coefficients will promote more comprehensive
479 and precise understandings on cell cycle- and autophagy-associated nanoparticle accumulation
480 (Table 2 and Table 3). Interestingly, if cells and nanoparticles were respectively considered as
481 individuals and therapeutic drugs, cell size-related and fluorescence intensity-based parameters
482 may remind us of similar parameters used in clinical practice alone or in combination, e.g.
483 total body surface area, mean body surface area, total body weight, body mass index, as well as
484 drug exposure- and drug dose-related parameters. On the other hand, as 3D assessment offers a
485 more comprehensive consideration of various factors, e.g. morphological changes during cell cycle
486 progression, disparities in cellular volume[45,46] and non-uniform intracellular distribution of
487 nanoparticles, 3D-based parameters might aid in mitigating the constraints associated with 2D level
488 and facilitates the "correction" of experimental findings. Further assessment of these parameters
489 based on a large amount of application data will not only deepen our understandings on their values
490 and significances, but also promote optimization of the technical platform constructed in this study.

491 Finally, although several issues warrant further investigation, e.g. detailed mechanisms
492 mediating cell cycle- and autophagy-associated nanoparticle accumulation, possible interplay
493 between cell cycle and autophagy, merits of TFI and MFI at different dimensional levels, as well
494 as possible nanoparticle- and cell line-mediated specificities on nanoparticle accumulation, our
495 findings may open new insights into optimizing the design and application of lipid-based and

496 possibly other nanomedicines besides providing a valuable technical solution. Particularly, around
497 3,200 LIP/LNP-based nano-formulations are currently under clinical investigations. In addition, it
498 is also notable that the technical platform constructed in this study may provide a new paradigm or
499 a new strategy for simultaneous investigation on other "effectors" in addition to cell cycle, or on
500 the basis of complete cell cycle phase separation.

Table 1. Cell cycle- and autophagy-associated accumulation patterns of DiD-LIP and DiD-LNP by cancer cells based on the multi-functional platform

Cell line	Dimension	DiD-LIP		DiD-LNP	
		TFI (a.u.)	MFI (a.u.)	TFI (a.u.)	MFI (a.u.)
WT PIP-FUCCI	2D	M < G1 ≈ S < G2	M < G1 ≈ S ≈ G2	M < G1 ≈ S < G2	M < G1 ≈ S < G2
	3D	M (≈ G1) < (G1 ≈) S < G2	M < G1 ≈ S ≈ G2	M < G1 ≈ S < G2	M < G1 < S < G2
ATG7 KO PIP-FUCCI	2D	M < G1 ≈ S < G2	M < G1 ≈ S ≈ G2	M < G1 ≈ S < G2	M < G1 ≈ S ≈ G2
	3D	M < G1 < S < G2	M < G1 ≈ S ≈ G2	M ≈ G1 ≈ S < G2	M < (G1 ≈) S < (G1 ≈) G2

TFI and MFI were first analyzed after $\log_{10}$ transformation. Statistical analysis among four distinct cell cycle phases was conducted using ANOVA with Bonferroni correction. ≈, no significant difference; TFI, total fluorescence intensity; MFI, mean fluorescence intensity; 2D, two-dimensional level; 3D, three-dimensional level.

Table 2. Spearman Correlation Coefficient between TFI (2D) and TFI (3D), MFI (2D) and MFI (3D) in WT and *ATG7* KO PIP-FUCCI cell lines

	WT PIP-FUCCI				***ATG7* KO PIP-FUCCI**			
	TFI (3D) of DiD-LIP	**TFI (3D) of DiD-LNP**	**MFI (3D) of DiD-LIP**	**MFI (3D) of DiD-LNP**	**TFI (3D) of DiD-LIP**	**TFI (3D) of DiD-LNP**	**MFI (3D) of DiD-LIP**	**MFI (3D) of DiD-LNP**
TFI (2D) of DiD-LIP	0.791 ($P < 0.0001$)	/	/	/	0.715 ($P < 0.0001$)	/	/	/
MFI (2D) of DiD-LIP	/	/	0.793 ($P < 0.0001$)	/	/	/	0.689 ($P < 0.0001$)	/
TFI (2D) of DiD-LNP	/	0.872 ($P < 0.0001$)	/	/	/	0.811 ($P < 0.0001$)	/	/
MFI (2D) of DiD-LNP	/	/	/	0.932 ($P < 0.0001$)	/	/	/	0.905 ($P < 0.0001$)

TFI, Total fluorescence intensity; MFI, Mean fluorescence intensity; DiD-LIP, DiD-labelled liposomes (at a dose equivalent to 5 μg/mL DOX); DiD-LNP, DiD-labelled lipid nanoparticles (at a dose equivalent to 6 μg/mL luciferase mRNA); 2D, Two-dimensional level; 3D, Three-dimensional level. The level of significance was set at $P < 0.05$.

Table 3. Spearman Correlation Coefficient between TFI (2D) and MFI (2D), TFI (3D) and MFI (3D) in WT and *ATG7* KO PIP-FUCCI cell lines

	WT PIP-FUCCI				***ATG7* KO PIP-FUCCI**			
	MFI (2D) of DiD-LIP	**MFI (2D) of DiD-LNP**	**TFI (3D) of DiD-LIP**	**TFI (3D) of DiD-LNP**	**MFI (2D) of DiD-LIP**	**MFI (2D) of DiD-LNP**	**TFI (3D) of DiD-LIP**	**TFI (3D) of DiD-LNP**
TFI (2D) of DiD-LIP	0.711 ($P < 0.0001$)	/	/	/	0.699 ($P < 0.0001$)	/	/	/
MFI (3D) of DiD-LIP	/	/	0.495 ($P < 0.0001$)	/	/	/	0.546 ($P < 0.0001$)	/
TFI (2D) of DiD-LNP	/	0.918 ($P < 0.0001$)	/	/	/	0.856 ($P < 0.0001$)	/	/
MFI (3D) of DiD-LNP	/	/	/	0.871 ($P < 0.0001$)	/	/	/	0.791 ($P < 0.0001$)

TFI, Total fluorescence intensity; MFI, Mean fluorescence intensity; DiD-LIP, DiD-labelled liposomes (at a dose equivalent to 5 μg/mL DOX); DiD-LNP, DiD-labelled lipid nanoparticles (at a dose equivalent to 6 μg/mL luciferase mRNA); 2D, Two-dimensional level; 3D, Three-dimensional level. The level of significance was set at $P < 0.05$.

References

1. Caster, J. M., Patel, A. N., Zhang, T. & Wang, A. Investigational nanomedicines in 2016: a review of nanotherapeutics currently undergoing clinical trials. *Wires. Nanomed. Nanobi.* **9**, e1416 (2017).
2. Mitchell, M. J. et al. Engineering precision nanoparticles for drug delivery. *Nat. Rev. Drug Discov.* **20**, 101–124 (2021).
3. Yechezkel (Chezy) Barenholz. Doxil® — The first FDA-approved nano-drug: Lessons learned. *J. Control. Release* **160**, 117–134 (2012).
4. Wang, H. Y. et al. Polyethylene glycol (PEG)-associated immune responses triggered by clinically relevant lipid nanoparticles in rats. *NPJ Vaccines* **8**, 169 (2023).
5. Zhivotovsky, B. & Orrenius, S. Cell cycle and cell death in disease: past, present and future. *J. Intern. Med.* **268**, 395–409 (2010).
6. Abouzeid, A. H. & Torchilin, V. P. The role of cell cycle in the efficiency and activity of cancer nanomedicines. *Expert Opin. Drug De.* **10**, 775–786 (2013).
7. Maleki, E. H., Bahrami, A. R. & Matin, M. M. Cancer cell cycle heterogeneity as a critical determinant of therapeutic resistance. *Genes Dis.* **11**, 189–204 (2024).
8. Sui, M. H., Dziadyk, J. M., Zhu, X. M. & Fan, W. M. Cell cycle-dependent antagonistic interactions between paclitaxel and γ-radiation in combination therapy. *Clin. Cancer Res.* **10**, 4848–4857 (2004).
9. Sui, M. H. & Xiong, X. X. Combination of gemcitabine antagonizes antitumor activity of paclitaxel through prevention of mitotic arrest and apoptosis. *Cancer Biol. Ther.* **5**, 1015–1021 (2006).
10. Sui, M. H. et al. G2 checkpoint abrogator abates the antagonistic interaction between antimicrotubule drugs and radiation therapy. *Radiother. Oncol.* **104**, 243–248 (2012).
11. Larson, N. et al. Biodegradable multiblock poly (N-2-hydroxypropyl) methacrylamide gemcitabine and paclitaxel conjugates for ovarian cancer cell combination treatment. *Int. J. Pharm.* **454**, 435-443 (2013).
12. Zhang, R., Yang, J. Y., Sima, M., Zhou, Y. & Kopeček, J. Sequential combination therapy of ovarian cancer with degradable N-(2-hydroxypropyl) methacrylamide copolymer paclitaxel and gemcitabine conjugates. *P. Natl. Acad. Sci. U. S. A.* **111**, 12181-12186 (2014).
13. Zheng, S. et al. Effects of cell cycle on the uptake of water soluble quantum dots by cells. *J. Appl. Phys.* **110**, 124701 (2011).
14. Wu, J. et al. Statistical single-cell analysis of cell cycle-dependent quantum dot cytotoxicity and cellular uptake using microfluidic system. *RSC Adv.* **4**, 24929–24934 (2014).
15. Patel, P. et al. Cell cycle dependent cellular uptake of zinc oxide nanoparticles in human epidermal cells. *Mutagenesis* **31**, 481–490 (2016).
16. Kim, J. A., Åberg, C., Salvati, A. & Dawson, K. A. Role of cell cycle on the cellular uptake and dilution of nanoparticles in a cell population. *Nat. Nanotechnol.* **7**, 62–68 (2012).

544 17. Go, E. J., Kim, E. J. & Hur, W. *In vitro* cellular uptake of fibroin microspheres and its dependency
545 on the cell cycle stage. *J. Microencapsul.* **30**, 124–131 (2013).
546 18. Huang, C. et al. Altered cell cycle arrest by multifunctional drug-loaded enzymatically-triggered
547 nanoparticles. *ACS Appl. Mater. Inter.* **8**, 1360–1370 (2016).
548 19. Tang, J. H. et al. The role of the cell cycle in the cellular uptake of folate-modified poly(L-amino
549 acid) micelles in a cell population. *Nanoscale* **7**, 20397–20404 (2015).
550 20. Su, L. J. et al. GRP75-driven, cell-cycle-dependent macropinocytosis of Tat/pDNA-Ca2+
551 nanoparticles underlies distinct gene therapy effect in ovarian cancer. *J. Nanobiotechnol.* **20**, 340
552 (2022).
553 21. Li, X. H., He, S. K. & Ma, B. Y. Autophagy and autophagy-related proteins in cancer. *Mol.*
554 *Cancer* **19**, 12 (2020).
555 22. Akin, D. et al. A novel ATG4B antagonist inhibits autophagy and has a negative impact on
556 osteosarcoma tumors. *Autophagy* **10**, 2021–2035 (2014).
557 23. Yang, S. H. et al. Pancreatic cancers require autophagy for tumor growth. *Gene Dev.* **25**, 717–
558 729 (2011).
559 24. Collier, J. J. et al. Emerging roles of ATG7 in human health and disease. *Embo. Mol. Med.* **13**,
560 e14824 (2021).
561 25. Manzanares, D. & Ceña, V. Endocytosis: the nanoparticle and submicron nanocompounds
562 gateway into the cell. *Pharmaceutics* **12**, 371 (2020).
563 26. Birgisdottir, Å. B. & Johansen, T. Autophagy and endocytosis – interconnections and
564 interdependencies. *J. Cell Sci.* **133**, jcs228114 (2020).
565 27. Zheng, W., Wei, M., Li, S. & Le, W. Nanomaterial-modulated autophagy: underlying
566 mechanisms and functional consequences. *Nanomedicine* **11**, 1417–1430 (2016).
567 28. Sipos, A. et al. Alveolar epithelial cell processing of nanoparticles activates autophagy and
568 lysosomal exocytosis. *Am. J. Physiol-Lung C.* **315**, L286–L300 (2018).
569 29. Sipos, A., Kim, K.-J., Sioutas, C. & Crandall, E. D. Evidence for nanoparticle-induced lysosomal
570 dysfunction in lung adenocarcinoma (A549) cells. *Int. J. Mol. Sci.* **20**, 5253 (2019).
571 30. Fageria, L. et al. Functional autophagic flux regulates AgNP uptake and the internalized
572 nanoparticles determine tumor cell fate by temporally regulating flux. *Int. J. Nanomedicine* **14**, 9063–
573 9076 (2019).
574 31. Guo, Q. et al. Hollow MIL-125 Nanoparticles Loading Doxorubicin Prodrug and 3-
575 Methyladenine for Reversal of Tumor Multidrug Resistance. *J Funct Biomater.* **14**, 546 (2023).
576 32. Yang, Y. et al. Application and interpretation of current autophagy inhibitors and activators. *Acta*
577 *Pharmacol. Sin.* **34**, 625–635 (2013).
578 33. Grant, G. D. et al. Accurate delineation of cell cycle phase transitions in living cells with PIP-
579 FUCCI. *Cell Cycle* **17**, 2496–2516 (2018).
580 34. Jackman, J. & O'Connor, P. M. Methods for synchronizing cells at specific stages of the cell
581 cycle. *Curr. Protoc. Cell Biol.* **8**, 8.3.1-8.3.20 (1998).

582 35. Doxil prescribing information. https://www.accessdata.fda.gov/drugsatfda_docs/label/2022/0
583 50718Orig1s060lbl.pdf (2022).
584 36. Comirnaty prescribing information. https://labeling.pfizer.com/ShowLabeling.aspx?id=16351
585 &format=pdf (2021).
586 37. Liu, R. F., Tang, J., Xu, Y. X. & Dai, Z. F. Bioluminescence imaging of inflammation
587 *in vivo* based on bioluminescence and fluorescence resonance energy transfer using nanobu
588 bble ultrasound contrast agent. *ACS Nano* **13**, 5124–5132 (2019).
589 38. Yang, L. et al. Live macrophage-delivered doxorubicin-loaded liposomes effectively treat triple-
590 negative breast cancer. *ACS Nano* **16**, 9799–9809 (2022).
591 39. Khare, P. et al. Lipid nanoparticle-mediated drug delivery to the brain. *Adv. Drug Deliver Rev.*
592 **197**, 114861 (2023).
593 40. Cadart, C. et al. Exploring the function of cell shape and size during mitosis. *Dev. Cell* **29**, 159–
594 169 (2014).
595 41. Nakayama, Motoshi. et al. Radiosensitivity of early and late M-phase HeLa cells isolated by a
596 combination of fluorescent ubiquitination-based cell cycle indicator (Fucci) and mitotic shake-off.
597 *Radiation Research.* **176**, 407-411 (2011).
598 42. Kessel, D. H., Price, M. & Reiners, Jr., J. J. ATG7 deficiency suppresses apoptosis and cell death
599 induced by lysosomal photodamage. *Autophagy* **8**, 1333–1341 (2012).
600 43. Li, W. et al. Phospholipid peroxidation inhibits autophagy via stimulating the delipidation of
601 oxidized LC3-PE. *Redox Biol.* **55**, 102421 (2022).
602 44. Taubenberger, A.V., Baum, B. & Matthews, H.K. The mechanics of mitotic cell rounding. *Front.*
603 *Cell Dev. Biol.* **8**, 687 (2020).
604 45. Needham, D. Possible role of cell cycle-dependent morphology, geometry, and mechanical
605 properties in tumor cell metastasis. *Cell Biophys.* **18**, 99–121 (1991).
606 46. Wang, Z.X. Regulation of cell cycle progression by growth factor-induced cell signaling. *Cells*
607 **10**, 3327 (2021).
608 47. Raucher, D. & Sheetz, M. P. Membrane expansion increases endocytosis rate during mitosis. *J.*
609 *Cell Biol.* **144**, 497–506 (1999).
610 48. Yang, Y.P. et al. Application and interpretation of current autophagy inhibitors and activators.
611 *Acta Pharmacol. Sin.* **34**, 625-635 (2013).
612 49. Park, E. J. et al. Chloroquine enhances TRAIL-mediated apoptosis through up-regulation of DR5
613 by stabilization of mRNA and protein in cancer cells. *Sci. Rep.* **6**, 22921 (2016).
614 50. Alber, A. B. & Suter, D. M. Dynamics of protein synthesis and degradation through the cell cycle.
615 *Cell Cycle* **18**, 784–794 (2019).
616 51. Li, Y. et al. APC/CCDH1 synchronizes ribose-5-phosphate levels and DNA synthesis to cell
617 cycle progression. *Nat. Commun.* **10**, 2502 (2019).

618 52. Zheng, Y., Su, C., Zhao, L. & Shi, Y.J. Chitosan nanoparticle-mediated co-delivery of shAtg-5
619 and gefitinib synergistically promoted the efficacy of chemotherapeutics through the modulation of
620 autophagy. *J. Nanobiotechnol.* **15**, 28 (2017).
621 53. Hu, C.L. et al. Co-delivery of the autophagy inhibitor si-Beclin1 and the doxorubicin nano-
622 delivery system for advanced prostate cancer treatment. *J. Biomater. Appl.* **36**, 1317-1331 (2022).
623

624 **Methods**

625 **Major reagents**

626 Cholesterol, 1-palmitoyl-2-stearoyl-sn-glycero-3-phosphocholine (HSPC), 1,2-distearoyl-sn-
627 glycero-3-phosphocholine (DSPC) and 1,2-distearoyl-sn-glycero-3-phosphoethanolamine-N-
628 [methoxy(polyethylene glycol)-2000] ($mPEG_{2000}$-DSPE) were from Lipoid GmbH (Ludwigshafen,
629 Germany). [(4-Hydroxybutyl)azanediyl]di(hexane-6,1-diyl) bis(2-hexyldecanoate) (ALC-0315) and
630 2-[(polyethylene glycol)-2000]-N,N-ditetradecylacetamide (ALC-0159) were acquired from
631 SINOPEG (Xiamen, China). 1,1′-Dioctadecyl-3,3,3′,3′-tetramethylindotricarbocyanine, 4-
632 chlorobenzenesulfonate salt (DiD) was from MKBio (Shanghai, China). Firefly luciferase mRNA
633 (LUC mRNA) was from Afana Biotechnology (Hefei, China). Ferric chloride hexahydrate and
634 ammonium thiocyanate were from Sigma-Aldrich (St. Louis, MO, USA). Lipofectamine 3000 and
635 Opti-MEM were purchased from Thermo Fisher Scientific (Waltham, MA, USA). Polybrene was
636 from Santa Cruz (Dallas, TX, USA). G418 was from InvivoGen (San Diego, CA, USA).
637 Glutaraldehyde, ethanol and acetone were from Hushi Chemical (Shanghai, China). Lead citrate was
638 from Macklin (Shanghai, China). RIPA buffer and DAPI staining solution were from Beyotime
639 (Shanghai, China). Proteases inhibitor and phosphatase inhibitor were from Yeason (Shanghai,
640 China). Protein marker was from BioRad (Hercules, CA, USA).

641 Lentivirus concentration kit (Cat. NO. 41101ES50) was acquired from Yeason. BCA protein
642 assay kit (Cat. NO. FD2001) was obtained from Thermo Fisher Scientific. E.Z.N.A. Endo-free
643 plasmid maxi kit (Cat. NO. D6926-03) was from Omega (Norcross, GA, USA). Plasmids of psPAX2
644 (Cat. NO. 12260), pMD2.G (Cat. NO. 12259), pLenti-PGK-Neo-PIP-FUCCI (PIP-FUCCI) (Cat. NO.
645 118616) and pLenti PGK Neo DEST (empty vector) (Cat. NO. 19067) were from Addgene
646 (Cambridge, MA, USA).

647 Anti-ATG7 antibody (Cat. NO. ab133528; clone name, EPR6251) and anti-SQSTM1/p62
648 antibody (Cat. NO. ab91526) were from Abcam (Waltham, MA, USA). LC3A/B XP Rabbit mAb

649 (Cat. NO. 12741S; clone name, D3U4C) and β-actin antibody (Cat. NO. 4967) were from Cell
650 Signaling Technology (Danvers, MA, USA). EpCAM monoclonal antibody, FITC (Cat. NO. MA1-
651 10197; clone name, VU-1D9), goat anti-rabbit IgG (H+L) highly cross-adsorbed secondary antibody
652 (Alexa Fluor 488) (Cat. NO. A32731), goat anti-rabbit IgG (H+L) cross-adsorbed secondary antibody
653 (Alexa Fluor 546) (Cat. NO. A11010), and goat anti-mouse IgG (H+L) cross-adsorbed secondary
654 antibody (Alexa Fluor 546) (Cat. NO. A11003) were from Thermo Fisher Scientific.
655

656 **Cell lines and cell cultures**

657 Wild type (WT) and *ATG7* knockout (*ATG7* KO) human osteosarcoma cancer cell lines U2OS were
658 kind gifts from Professor Qiming Sun at Zhejiang University School of Medicine. Human kidney
659 epithelial cell line 293T was from the Shanghai Institute of Cells, Chinese Academy of Sciences. All
660 cell lines, including newly established WT and *ATG7* KO PIP-FUCCI cell lines (see below section),
661 were authenticated by STR profiling (Tsingke Biotechnology, Beijing, China) and confirmed to be
662 mycoplasma free. All cell lines were in cultured in DMEM supplemented with 10% (v/v) fetal bovine
663 serum and maintained at 37 °C in an atmosphere containing 5% CO_2.
664

665 **Preparation of model nanoparticles DiD-LIP and DiD-LNP**

666 DiD-LIP was synthesized according to the officially published formulation of Doxil®[35] and previous
667 reports[54]. First, HSPC, cholesterol and $mPEG_{2000}$-DSPE, at 56.6:38.1:5.3 molar ratio, were hydrated
668 in 10 mM sucrose-histidine buffer at pH6.5. Subsequently, DiD was added into the lipid mixture at a
669 concentration of 0.4 mol%, followed by vortex at 60 °C for 2-3 minutes to generate multilamellar
670 vesicles (MLVs). Finally, the MLVs were reduced in size using 400, 100, 80, and 50 nm-pore size
671 polycarbonate filters with a 10-mL extruder barrel (Northern Lipids, Vancouver, Canada), and stored
672 at a temperature of 2-8 °C until use.

673 DiD-LNP was prepared based on the officially published formulation of Comirnaty®[36] using a
674 modified procedure we previously described[4,55]. Initially, ALC-0315, DSPC, cholesterol and ALC-
675 0159 were dissolved at a molar ratio of 46.3: 9.4: 42.7: 1.6 to fabricate the ethanol phase and DiD
676 was then added into the lipids at a concentration of 0.4 mol%. Meanwhile, LUC mRNA was dissolved
677 in 20 mM citrate buffer to prepare the aqueous phase. Subsequently, the above two phases were mixed

678 with a microfluidic mixer (Precision Nanosystems, Canada) at a flow rate ratio of 1:3 (ethanol:
679 aqueous). Afterwards, the resulting nanoparticle solution was subjected to dialysis against 10 ×
680 volume of PBS for at least 18 hours using tangential flow filtration (TFF) membranes with molecular
681 weight cut-offs of 100 kD (Sartorius Stedim, Germany). With the assistance of an Amicon
682 ultracentrifugal filter (EMD Millipore, Billerica, MA, USA), the nanoparticle solution was passed
683 through a 0.22 μm filter and ultimately concentrated to the desired concentration.
684
685 **General characterization of DiD-LIP and DiD-LNP**
686 As we previously introduced in details[4], a Zetasizer Nano ZS instrument (Malvern Instruments Ltd,
687 Malvern, UK) was employed to measure hydrodynamic size (Z-average), polydispersity index (PDI)
688 and zeta potential of DiD-LIP and DiD-LNP, with the temperature maintained at 25 °C throughout
689 the testing period. To further evaluate their stability in experimental environment, DiD-LIP and DiD-
690 LNP were diluted with cell culture solution and incubated at 37 °C for 24 hours. Afterwards,
691 nanoparticle samples were respectively collected at specified time points (1 hour, 2 hours, 6 hours,
692 12 hours and 24 hours post-incubation). Except that the test temperature was changed to 37 °C,
693 samples collected were subjected to aforementioned characterization of Z-average and PDI.
694 Moreover, morphology of DiD-LIP and DiD-LNP was examined with Cryo-TEM, with images
695 captured with a Talos F200C instrument (FEI/Thermo Scientific, Waltham, MA, USA) equipped with
696 a Ceta 4k × 4k camera at an acceleration voltage of 200 kV. Moreover, the phospholipid (HSPC and
697 $mPEG_{2000}$-DSPE) concentration of DiD-LIP solutions and phospholipid (DSPC) concentration of
698 DiD-LNP solutions were determined through Steward's assay as previously described in details[4,56,57].
699 Eventually, calibration curves were established for DSPC lipids within the range of 25 to 200 μg/mL,
700 and for HSPC lipids within the range of 25 to 150 μg/mL. These curves were applied to determine
701 the ultimate concentrations of phospholipids in the DiD-LIP and DiD-LNP solutions. Three separate
702 experiments were conducted for further statistical analysis. According to previous pharmacokinetics
703 studies and related literatures, the doses of DiD-LIP and DiD-LNP used in this study were equivalent
704 to 5 μg/mL DOX [35,58,59] (42.67 μg/mL of lipids including 25.61 μg/mL of HSPC, 8.53 μg/mL of
705 $mPEG_{2000}$-DSPE and 8.53 μg/mL of Cholesterol) and 6 μg/mL LUC mRNA [60-62] (154.20 μg/mL of

706 lipids including 85.80 μg/mL of ALC-0315, 10.20 μg/mL of ALC-0159, 18.00 μg/mL of DSPC and
707 40.20 μg/mL of Cholesterol), respectively. Same volume of PBS was used as a control.
708

709 **Construction of isogenic WT and *ATG7* KO PIP-FUCCI cell lines stably expressing cell cycle**
710 **indicator PIP-FUCCI**

711 As previously reported, in the cell cycle indicator plasmid PIP-FUCCI, mVenus fluorescent protein
712 was fused to the PCNA-interacting protein (PIP) degron of human *Cdt1* gene ($Cdt1_{1\text{-}17}$), which is
713 rapidly degraded at the onset of DNA replication[33]. Meanwhile, mCherry fluorescent protein was
714 fused to the *Geminin* gene ($Gem_{1\text{-}110}$), which accumulates during S-phase, G2-phase and M-phase and
715 begins to be degraded at late M-phase[33,63]. Based on these characteristics, Grant et al. demonstrated
716 that in U2OS cell line transfected with PIP-FUCCI, mVenus single-positive cells displaying green
717 nuclear fluorescence are at G1-phase, mCherry single-positive cells displaying red nuclear
718 fluorescence are at S-phase, while mVenus and mCherry double-positive cells displaying yellow
719 (overlap of green and red) nuclear fluorescence are at either G2-phase or M-phase[33].

720 To take the advantage of cell cycle indicating capability of PIP-FUCCI plasmid in living cells,
721 hereby WT and *ATG7* KO U2OS cell lines were stably transfected with PIP-FUCCI. Briefly, 1×10^6
722 293T cells were cultured into a 10-cm dish for overnight incubation. For lentiviral transduction,
723 Lipofectamine 3000 was used to co-transfect PIP-FUCCI plasmid, psPAX2 and pMD2.G plasmids
724 into 293T cells, with empty vector serving as a negative control. The medium was replaced 6-8 hours
725 after transfection, and was harvested and concentrated at 72 hours post-transfection. Afterwards,
726 approximately 6×10^4 exponentially growing WT and *ATG7* KO U2OS cells were respectively
727 seeded into cell culture plates. After overnight incubation, cells were exposed to concentrated
728 lentiviral supernatant containing either PIP-FUCCI or empty vector, along with 8 μg/mL polybrene.
729 Transduced cells were then selected for around one week with 500 μg/mL of G418. WT and *ATG7*
730 KO U2OS cells expressing the empty vector, so called WT and *ATG7* KO Vector cell lines
731 respectively, were amplified for subsequent experiments, while those transfected with PIP-FUCCI
732 were sorted by BD FACSAria II flow cytometry (BD Biosciences, CA, USA) to obtain WT and *ATG7*
733 KO PIP-FUCCI cell lines exhibiting strong mVenus and/or mCherry fluorescence for further studies.
734

735 **Cell-cycle phase tracking of WT and *ATG7* KO PIP-FUCCI cells through time-lapse live-cell**
736 **imaging.**
737 Approximately 8×10^4 exponentially growing WT and *ATG7* KO PIP-FUCCI cells were seeded into
738 confocal dishes for overnight incubation. Live-cell imaging was conducted using an Andor BC43
739 spinning disk confocal microscope (Oxford Instruments, Abingdon, UK) at 20 × magnification (0.8
740 NA) for a duration of up to 25 hours, corresponding to the estimated cell doubling time
741 (Supplementary Fig. 5). The imaging was performed under controlled conditions of 5% CO_2 and
742 37 °C, with images acquired at 5-minute intervals.
743
744 **Evaluation of the influence of PIP-FUCCI transfection on cell morphology and proliferation**
745 WT and *ATG7* KO Vector cell lines, as well as WT and *ATG7* KO PIP-FUCCI cell lines were
746 carefully checked with light microscope for morphological examination. In addition, these cell lines
747 were respectively seeded into 6-well plates (1×10^5 cells for each well). A Countess II FL Automated
748 Cell Counter (Thermo Fisher Scientific) was employed for five consecutive cell number counting
749 between 24 hours and 120 hours after seeding, with a 24-hour interval. Cell doubling time of each
750 cell line was calculated according to the following equation: Doubling time = Duration time of cell
751 culture × $\log_{10}$ (2)/[$\log_{10}$ (final cell number) – $\log_{10}$ (initial cell number)].
752
753 **Cell cycle distribution detected by flow cytometry**
754 Exponentially growing WT and *ATG7* KO PIP-FUCCI cells were seeded at a density of 1×10^6 cells
755 per 10-cm dish and cultured overnight. Cells were then respectively administered with DiD-LIP and
756 DiD-LNP for 2 hours. Afterwards, cells were first gently shaken (so called mitotic shake-off) and the
757 culture medium containing floating mitotic cells was harvested separately. Then, the remaining
758 adherent G1-phase, S-phase and G2-phase cells were harvested after digestion with trypsinization. In
759 addition, exponentially growing WT and *ATG7* KO PIP-FUCCI cells were seeded at 3×10^5 cells per
760 well into 6-well plates and cultured overnight. Cells were then respectively administered with DiD-
761 LIP and DiD-LNP for 12 hours, 24 hours and 48 hours. Afterwards, cells were routinely harvested
762 with trypsinization, rinsed three times with PBS. Each cell sample was suspended in 1 mL of DAPI
763 staining solution and subsequently analyzed in equal volumes with a CytoFLEX LX (Beckman

764 Coulter, Indianapolis, USA) to determine the cell cycle distribution. DAPI, mVenus and mCherry
765 channels were respectively excited with 375 nm, 488 nm and 561 nm lasers, and detected with
766 corresponding 450/45 nm, 525/40 nm and 610/20 nm bandpass filters. As described above, cancer
767 cells exhibited the following cell cycle-dependent fluorescence: G1-phase (mVenus positive), green
768 fluorescence; S-phase (mCherry positive), red fluorescence; G2-phase and M-phase (mVenus and
769 mCherry double-positive), yellow fluorescence.
770
771 **Examination of possible effects of nanoparticles on autophagic vesicle formation with TEM**
772 Exponentially growing WT and *ATG7* KO PIP-FUCCI cells were seeded at 7×10^5 cells per 6-cm
773 culture dish for overnight incubation. Cells were then respectively administered with DiD-LIP and
774 DiD-LNP for 2 hours. Following overnight fixation with 2.5% glutaraldehyde, cells underwent three
775 washes with PBS for a duration of 10 minutes each. Subsequently, cells were subjected to fixation
776 with 1% osmium tetroxide for 1 hour, followed by rinsing with PBS prior to staining with 2% uranyl
777 acetate for 30 minutes. For dehydration, samples were respectively placed in 50%, 70%, 90% and
778 100% ethanol for 15 minutes and then in 100% acetone for 20 minutes twice. Afterwards, a Leica
779 UC7 microtome (Leica, Solms, Germany) was used to prepare ultrathin sections and sample staining
780 were performed with lead citrate and uranyl acetate. Photographs of autophagic vesicles were
781 captured using a Tecnai 10 TEM (Philips, Amsterdam, Netherlands) at 100 kV. At least 10 cells were
782 randomly chosen from each group for imaging and statistical analysis.
783
784 **Western blotting to assess possible effects of nanoparticles on autophagy-related proteins**
785 Exponentially growing WT and *ATG7* KO PIP-FUCCI cells were seeded at 7×10^5 cells per 6-cm
786 culture dish for overnight incubation. Cells were then respectively administered with DiD-LIP and
787 DiD-LNP for 2 hours. Then cells were harvested with trypsinization, rinsed three times with PBS and
788 subjected to RIPA buffer containing proteases and phosphatase inhibitors on ice for 10 minutes.
789 Subsequently, the supernatant was collected through centrifugation at 12,000 × g for 20 minutes.
790 Protein concentrations were determined with a BCA protein assay kit. A gel of 15% SDS-PAGE was
791 used to electrophorese proteins (40 μg /lane) prior to being transferred onto a PVDF membrane. After
792 blocking with 5% (w/v) bovine serum albumin for 1 hour, the membranes were incubated with

793 following antibodies overnight at 4 °C: anti-ATG7 (1:1,000 dilution), anti-SQSTM1/p62 (1:1,000
794 dilution), anti-MAP1LC3A/B (1:1,000 dilution) and anti-β-actin (1:5,000 dilution). Next, membranes
795 were rinsed with TBS solution containing 0.1% (v/v) Tween 20 and incubated with corresponding
796 secondary antibodies (1:5,000 dilution) for 2 hours. Odyssey imaging system was employed for WB
797 imaging (LI-COR Biosciences, Lincoln, USA).
798

799 **Integration of PIP-FUCCI expression with mitotic shake-off for distinguishment and collection**
800 **of cells at four cell cycle phases and determination of cell cycle-associated nanoparticle**
801 **accumulation**

802 Approximately 8×10^4 exponentially growing WT and *ATG7* KO PIP-FUCCI cells were seeded into
803 confocal dishes for overnight incubation. Then cells were administered with DiD-labelled model
804 nanoparticles (blue intracellular fluorescence in CLSM) at designated doses and incubated for 1.5
805 hours. Afterwards, cells were incubated with 25 μL FITC-EpCAM monoclonal antibody for
806 additional 30 minutes to draw the outline of cell membrane (green cell membrane fluorescence in
807 CLSM) and meanwhile exclude apoptotic cells or cell debris.

808 It should be noted that the use of PBS rinses to remove above unbound nanoparticles and
809 antibody prior to subsequent nanoparticle fluorescence detection results in the loss of a large
810 proportion of M-phase cells. Fortunately, unique properties of typical M-phase cells, e.g. spherical
811 shape and significantly decreased adhesion capability[41] facilitate convenient separation by gentle
812 mitotic shake-off[34], through which a complete distinguishment and adequate collection of cells at four
813 cell cycle phases were successfully achieved by integrating PIP-FUCCI with mitotic shake-off in this
814 study.

815 To achieve complete separation and adequate collection of cells at four different cell cycle
816 phases, cells cultured in confocal dishes were gently shaken, and the culture medium containing
817 floating mitotic cells was harvested with sterile centrifuge tubes, then settled and concentrated mitotic
818 cells were transferred into another new confocal dish. Both the adherent G1-phase (mVenus single-
819 positive, green nuclear fluorescence in CLSM), S-phase (mCherry single-positive, red nuclear
820 fluorescence in CLSM) and G2-pahse (mVenus and mCherry double-positive, yellow nuclear
821 fluorescence in CLSM) cells remained in original confocal dishes, and the floating M-phase cells

822 (mVenus and mCherry double-positive, yellow nuclear fluorescence in CLSM) harvested separately
823 via mitotic shake-off into new dishes were gently rinsed three times with PBS to remove unbound
824 fluoroprobes, before examination with high-resolution CLSM and 3D reconstruction technique (see
825 below section). It is noteworthy that although the emission wavelength of FITC partially overlaps
826 with that of mVenus, FITC-labeled EpCAM expresses on the cell membrane as an epithelial cell
827 adhesion molecule[64], whereas mVenus expresses in the nucleus[33]. Consequently, there is no
828 interference between them due to distinct expression locations.
829

830 **High-resolution CLSM and 3D reconstruction technique for multi-dimensional evaluation of**
831 **cell cycle- and autophagy-associated nanoparticle accumulation**

832 Successful construction of WT and *ATG7* KO PIP-FUCCI cell lines and achievement of complete
833 cell cycle phase separation have provided us with the opportunity to simultaneously determine cell
834 cycle- and autophagy-associated cellular accumulation of DiD-labelled model nanoparticles. Live-
835 cell imaging was conducted using the Confocal Zeiss LSM 880 (Carl Zeiss, Jena, Germany) equipped
836 with a 63 × oil immersion objective (1.40 NA) with a resolution of 2048 × 2048 pixels, together with
837 an incubation chamber set at 37 °C and 5% CO_2. Filter sets were as follows: mVenus (excitation: 514
838 nm, emission: 519–590 nm), mCherry (excitation: 561 nm, emission: 570–620 nm), DiD (excitation:
839 633 nm, emission: 638–756 nm) and FITC (excitation: 488 nm, emission: 500–550 nm)[33]. In addition
840 to labelling cell membrane with FITC, morphological examination of cell with bright field was
841 helpful in identifying typical and healthy M-phase cells with intact and smooth cell membranes.

842 Besides regular two-dimensional (2D) CLSM imaging to determine the cell cycle phase and
843 nanoparticle accumulation, three-dimensional (3D) imaging was also conducted by acquiring 30-80
844 μm z-stacks at z-step intervals of 0.4-1 μm. DiD-LIP and DiD-LNP were respectively added into cells,
845 using same volume of PBS as a control. DiD fluorescence was detected under identical conditions
846 for both control groups and nanoparticle-treated groups, with background intensity determined
847 according to DiD fluorescence detected in corresponding control groups. Following delineation of
848 cell boundaries in 2D images using brightfield and FITC fluorescence, TFI of intracellular DiD was
849 quantified using Fiji/Image J (imagej.nih.gov). Subtraction of the background intensity yielded TFI
850 (2D) of DiD in experimental cells. To eliminate variations in TFI (2D) due to differences in cell area,

851 mean fluorescence intensity (MFI) of intracellular DiD at the 2D level, so called MFI (2D), was
852 calculated as the ratio of TFI (2D) vs. cell area[65]. Imaris software (Bitplane) was used to reconstruct
853 3D images of confocal z-stacks, with a series of parameters such as Surface Grain Size and Manual
854 Threshold Value parameters maintained consistent during signal processing to determine TFI of
855 intracellular DiD. Similarly, TFI (3D) was obtained based on TFI of DiD subtracting the background
856 intensity To eliminate variations in TFI (3D) due to differences in cell volume, TFI (3D) was divided
857 by corresponding cell volume to obtain MFI (3D)[66].
858
859 **Correlation analysis and comparison of correlations among groups**
860 Pearson correlation coefficients were employed to evaluate the correlations between TFI (3D) and
861 cell volume, and Spearman correlation coefficients were employed to evaluate the correlations
862 between multi-dimensional TFI and MFI parameters. Correlations with $P < 0.05$ were considered
863 significant and the degree of correlation was assessed using correlation coefficient (r) (r values, 0.00
864 ~ < 0.03, negligible correlation; 0.30 ~ < 0.50, low correlation; 0.50 ~ < 0.70, moderate correlation;
865 0.70 ~ < 0.90, high correlation and 0.90 ~ < 1.00, very high correlation)[67]. In addition, comparison of
866 correlations among groups was compared with a z-test on Fisher z-transformation, and $P < 0.05$ was
867 considered significant[68].
868
869 **Data presentation and statistical analysis**
870 Data were presented as "mean ± standard deviation". Since the normality test for continuous
871 parametric data is a prerequisite for determining the statistical analysis method[4,69,70], Shapiro-Wilk
872 test was used to evaluate normality. Nonparametric tests generally have lower statistical power
873 compared to parametric tests, especially in studies with small sample sizes[71]. Therefore, when the
874 normal distribution of original or transformed data were confirmed, parametric tests were conducted.
875 Otherwise, nonparametric tests were used. Parametric tests, One-way analysis of variance (ANOVA)
876 with Bonferroni correction and an independent t-test were conducted for analyzing possible changes
877 on nanoparticle stability and cell cycle distribution. Mann-Whitney U test (nonparametric test) was
878 employed to analyze statistical differences in autophagic vesicle number among various groups. In
879 addition, the raw data of cell area, cell volume, TFI and MFI of DiD-LIP/DiD-LNP at different

880 dimensional levels, exhibited a partially non-normal distribution. However, they became a normal
881 distribution after $\log_{10}$ transformation. Thus, the above raw data were transformed prior to statistical
882 analyses, their differences among four distinct cell cycle phases were conducted using ANOVA with
883 Bonferroni correction, and their differences between WT and *ATG7* KO PIP-FUCCI cell lines were
884 evaluated with an independent sample *t*-test. All statistical analyses were conducted using SPSS 21.0
885 (IBM SPSS, Chicago, USA). $P < 0.05$ is considered statistically significant.
886
887 **References**

888 54. Bavli, Y. et al. Doxebo (doxorubicin-free Doxil-like liposomes) is safe to use as a pre-treatment
889 to prevent infusion reactions to PEGylated nanodrugs. *J. Control. Release* **306,** 138–148 (2019).
890 55. Zhang, N. N. et al. A Thermostable mRNA Vaccine against COVID-19. *Cell* **182**, 1271-1283.
891 (2020).
892 56. Stewart, J. C. M. Colorimetric determination of phospholipids with ammonium ferrothiocyanate.
893 *Anal. Biochem.* **104**, 10–14 (1980).
894 57. Bandyopadhyay, A., McCarthy, K. A., Kelly, M. A. & Gao, J. Targeting bacteria via
895 iminoboronate chemistry of amine-presenting lipids. *Nat. Commun.* **6**, 6561 (2015).
896 58. Li, Y. J. et al. Thermal-responsive carbon monoxide (CO) delivery expedites metabolic
897 exhaustion of cancer cells toward reversal of chemotherapy resistance. *ACS Central Sci.* **5**, 1044-
898 1058 (2019).
899 59. Shi, C.Y. et al. A drug-specific nanocarrier design for efficient anticancer therapy. *Nat. Commun.*
900 **6**, 7449 (2015).
901 60. Parhiz, H. et al. PECAM-1 directed re-targeting of exogenous mRNA providing two orders of
902 magnitude enhancement of vascular delivery and expression in lungs independent of apolipoprotein
903 E-mediated uptake. *J. Control. Release* **291**, 106-115 (2018).
904 61. Paunovska, K. et al. Increased PIP3 activity blocks nanoparticle mRNA delivery. *Sci. Adv.* **6**,
905 5672 (2020).
906 62. Maugeri, M. et al. Linkage between endosomal escape of LNP-mRNA and loading into EVs for
907 transport to other cells. *Nat. Commun.* **10**, 4333 (2019).
908 63. McGarry, T. J. & Kirschner, M. W. Geminin, an inhibitor of DNA replication, is degraded during
909 mitosis. *Cell* **93**, 1043–1053 (1998).
910 64. Jing, Y. Y. et al. Quantitatively mapping the assembly pattern of EpCAM on cell membranes
911 with peptide probes. *Anal. Chem.* **92**, 1865–1873 (2020).
912 65. Shen, X. et al. MiR-322/-503 rescues myoblast defects in myotonic dystrophy type 1 cell model
913 by targeting CUG repeats. *Cell Death Dis.* **11**, 891 (2020).
914 66. Trivedi, P. et al. The inner centromere is a biomolecular condensate scaffolded by the
915 chromosomal passenger complex. *Nat. Cell Biol.* **21**, 1127–1137 (2019).

916 67. Mukaka, M. M. Statistics corner: A guide to appropriate use of correlation coefficient in medical
917 research. *Malawi Med J.* **24**, 69-71 (2012).
918 68. Abeler-Dörner, Lucie. et al. High-throughput phenotyping reveals expansive genetic and
919 structural underpinnings of immune variation. *Nat Immunol.* **21**, 86-100 (2020).
920 69. Zamecnik, C. R. et.al. An autoantibody signature predictive for multiple sclerosis. *Nat Med.* **30**,
921 1300-1308 (2024).
922 70. Beharier, O. et.al. Efficient maternal to neonatal transfer of antibodies against SARS-CoV-2 and
923 BNT162b2 mRNA COVID-19 vaccine. J Clin Invest. 131, e154834 (2021).
924 71. Nahm, F. S. Nonparametric statistical tests for the continuous data: the basic concept and the
925 practical use. *Korean J Anesthesiol.* **69**, 8-14 (2016)
926

927 **Acknowledgments**

928 This work was supported by grants from Zhejiang Provincial Natural Science Foundation of China
929 (LZ23E030003 to Dr. Meihua Sui), the National Natural Science Foundation of China (21722405
930 and 22075243 to Dr. Meihua Sui) and Startup Foundation for Hundred-Talent Program of Zhejiang
931 University (to Dr. Meihua Sui). We would like to acknowledge Dr. Yingjie Wang, Dr. Wei Liu, Dr.
932 Yongzhong Du and Dr. Qiming Sun at Zhejiang University for insightful discussions. In addition, we
933 would like to acknowledge Shenghai Chang, Lingyun Wu and Beibei Wang in the Center of Cryo-
934 Electron Microscopy (CCEM), Zhejiang University for their technical assistance on Cryo-EM and
935 TEM. We would like to acknowledge Shuangshuang Liu, Guifeng Xiao and Yueting Xing from the
936 Core Facilities, Zhejiang University School of Medicine for their technical assistance on confocal
937 live imaging, 3D reconstruction and flow cytometry. We would also like to acknowledge Yina Wang
938 for her assistance on language polishing.
939

940 **Author contributions**

941 M.S., the principal investigator of the major supporting grants, and Y.W. conceived the study and
942 defined the goals of the present study. M.S., Y.W., G.L. and H.W. designed the experiments. Y.W.,
943 G.L. and H.W. performed the research. X.X. provided technical/platform supports. M.S., Y.W., G.L.,
944 H.W., Y.Z., W.Z., J.L., B.C. and Y.J. discussed this project and analyzed the data. M.S., Y.W., G.L.

and H.W. drafted the manuscript. M.S., Y.W., G.L., H.W., Y.Z., W.Z., J.L., B.C. and Y.J. revised and edited the manuscript. These authors contributed equally: Y.W., G.L. and H.W.

Competing interests

The authors declare no competing interests.

Data availability

All data supporting the findings of this study are available within the paper and Supplementary Information. The associated raw data are available from the corresponding author on reasonable request.

Correspondence and requests for materials should be addressed to Meihua Sui.